

LMC-driven anisotropic boosts in stream–subhalo interactions

ARPIT ARORA ¹, NICOLÁS GARAVITO-CAMARGO ², ROBYN E. SANDERSON ^{1,2}, EMILY C. CUNNINGHAM ^{3,2,*}, ANDREW WETZEL ⁴,
NONDH PANITHANPAISAL ^{1,5,6} AND MEGAN BARRY ⁴

¹*Department of Physics & Astronomy, University of Pennsylvania, 209 S 33rd St, Philadelphia, PA 19104, USA*

²*Center for Computational Astrophysics, Flatiron Institute, 162 5th Ave, New York, NY 10010, USA*

³*Department of Astronomy, Columbia University, 550 West 120th Street, New York, NY 10027, USA*

⁴*Department of Physics & Astronomy, University of California, Davis, CA 95616, USA*

⁵*Carnegie Observatories, 813 Santa Barbara St, Pasadena, CA 91101, USA*

⁶*TAPIR, California Institute of Technology, Pasadena, CA 91125, USA*

(Received XXX; Revised XXX; Accepted XXX)

Submitted to APJ

ABSTRACT

Dark matter (DM) subhalos are predicted to perturb stellar streams; stream morphologies and dynamics can constrain the mass distribution of subhalos. Using FIRE-2 simulations of Milky Way-mass galaxies, we show that presence of a Large Magellanic Cloud (LMC)-analog significantly changes stream-subhalo encounter rates. Three key factors drive these changes. First, the LMC-analog brings in many subhalos, increasing encounter rates for streams near the massive satellite by up to 20–40%. Second, the LMC-analog displaces the host from its center-of-mass (inducing reflex motion), causing a north-south asymmetry in the density and radial velocity distributions of subhalos. This asymmetry results in encounter rates varying by 50–70% across the sky at the same distance. Finally, the LMC-mass satellite induces a density wake in the host’s DM halo, further boosting the encounter rates near the LMC-analog. We also explore the influence of stream orbital properties, finding a 50% increase in encounters for streams moving retrograde to the LMC-analog’s orbit in the opposite hemisphere. The dependence of encounter rates on stream location and orbit has important implications for where to search for new streams with spurs and gaps in the Milky Way.

Keywords: stellar streams, dark matter, Large Magellanic Cloud

1. INTRODUCTION

A promising indirect method to constrain the nature of dark matter (DM) is by measuring the mass function of dark subhalos. At these small scales, different DM models (that have yet to be ruled out observationally) have different predictions for the number of expected subhalos as a function of mass. For example, in the cold dark matter (CDM) paradigm, the predicted number of dark subhalos at the low-mass end ($10^7 M_{\odot}$) for a galaxy like the Milky Way (MW) is approximately 10^3 subhalos, while in warm dark matter (WDM) models the expected number depends on the mass of the WDM particles and ranges from $10 - 10^3$ dark subhalos (e.g., Kim et al. 2018). In self-interacting DM models with velocity dependent cross-section and maximum transfer cross-section

of about $3.5 \text{ cm}^2 \text{ g}^{-1}$, we expect around 100 subhalos (e.g., Vogelsberger et al. 2012; Robles et al. 2019). Thus, measuring the abundance of subhalos at mass scales below $10^7 M_{\odot}$ would provide strong constraints between different DM models. A promising way to detect subhalos in the MW is by observing their signatures after they interact with cold substructures such as stellar streams (Johnston et al. 2002; Erkal & Belokurov 2015a; Sanders et al. 2016; Bovy et al. 2017; Malhan et al. 2021). The prime example is the GD-1 stream, a long (10 kpc, approximately 100°) and thin (20 pc) stream around the MW (Grillmair & Dionatos 2006). The density of the stream is not smooth, but rather shows several gaps in density, one overdensity, and stars orbiting with the stream above the main stream track, known as “the spur” (Price-Whelan & Bonaca 2018; Malhan et al. 2019). Detailed orbital modeling has constrained the mass of the perturber to be $10^6 - 10^8 M_{\odot}$, possibly originating as a subhalo brought by the Sagittarius dwarf galaxy (Bonaca et al. 2019). However, the concentration of this perturber is only marginally consistent with predictions for CDM subhalos (de Boer et al.

Corresponding author: Arpit Arora
arora125@sas.upenn.edu

* NASA Hubble Fellow

2020). These results have motivated searches for further observational evidence of stream–subhalo interactions across the MW’s halo.

Currently, there are about 100 known streams in the MW (Mateu 2023) located at different distances and in different regions of the sky, providing a unique opportunity to detect the signatures of dark subhalos across the galaxy. Surveys such as Gaia (Collaboration et al. 2016b), DESI (Collaboration et al. 2016a), H3 (Conroy et al. 2019), the Vera Rubin Observatory (Ivezić et al. 2019), WEAVE (Dalton et al. 2012), 4most (De Jong et al. 2019), and Subaru PFS (Takada et al. 2014), among others, will further observe streams all the way to the edge of the galaxy and in external galaxies (Pearson et al. 2022; Aganze et al. 2023). The data from all of these surveys will provide a multidimensional view (kinematics and chemistry) of the stellar halo that will allow the detection and characterization of the morphology of stellar streams and, hence, the detection low-mass, completely dark subhalos.

Assuming that more perturbed streams can be found, and their perturbers constrained with dynamical modeling, obtaining constraints on the properties of the DM particle from these few perturbers requires interpreting their consistency with the population of subhalos predicted for each DM model. The usual practice currently is to assume that the DM subhalo population is isotropic (e.g. Carlberg 2009; Yoon et al. 2011; Bovy 2016; Erkal & Belokurov 2015b; Sanders et al. 2016). However, the Milky Way’s distribution of satellite galaxies and subhalos is almost certainly *anisotropic* (e.g. Pawłowski & Kroupa 2020; Li et al. 2021a; Savino et al. 2022). One of the main causes of this anisotropic distribution is the anisotropic accretion through filaments (Libeskind et al. 2011) and recent accretion of the Magellanic Clouds, here we will focus on the effect from these massive satellites, which are causing several disequilibria throughout the galaxy (e.g., see Vasiliev 2023, for a recent review). In short, the LMC brings its own subhalos distributed along the DM debris (e.g., Deason et al. 2015; Wetzel et al. 2015; Sales et al. 2017), displaces the host from its center-of-mass (inducing reflex motion), causing a north-south asymmetry in the density and radial velocity distributions (e.g., Garavito-Camargo et al. 2019; Petersen & Peñarrubia 2020; Erkal et al. 2019), and induce a DM density wake in the host’s DM halo (Garavito-Camargo et al. 2019) and stellar halo (Cunningham et al. 2020; Conroy et al. 2021). As a result, streams located in different locations in the sky but at the same galactocentric distance would experience different interaction rates with DM subhalos.

Recently, Barry et al. (2023) calculated the enhancements effect of LMC-mass satellites on several subhalo population metrics, including the number density and orbital flux. They found that the presence of an LMC-mass satellite enhances these population metrics by up to factors of 1.2–2. In this paper, we quantify the effect of massive LMC-mass satellite on the subhalo–stream interaction in one of the systems which is most LMC-like in its orbit and mass ratios at first pericenter. By using the Latte suite of FIRE-2 simulations (Wetzel et al. 2016, 2023), we predict which regions in the halo would have higher subhalo-stream interactions.

The structure of this paper is as follows: In Sec. 2, we provide a detailed explanation of our choice of zoomed-in cosmological FIRE-2 simulations. We identify the closest MW-LMC analog in FIRE-2 suite and establish the analytical models to compute stream–subhalo encounter rates. Additionally, we demonstrate how we inject both real MW and synthetic streams and integrate their orbits to calculate encounter rates. In Sec. 3, we investigate the impact of in-falling satellites and the MW’s response on encounter rates. We analyze key parameters influencing these rates, including the DM wake, collective response, and reflex motion. In Sec. 4, we present the computed encounter rates for both synthetic streams and injected MW streams. Statistical analysis is used to highlight key differences observed in the encounter rates, which are dependent on stream properties and their local positions. Finally, in Sec. 5, we discuss the implications of our results in the context of the MW. Our conclusions are presented in Sec. 6.

2. STREAM-SUBHALO ENCOUNTERS IN SIMULATIONS

In this section, we detail our approach to studying stream–subhalo encounters in simulations. We begin by explaining our choice of simulations and the methodology for identifying the LMC-analog in our simulations. Next, we establish Galactocentric and stream-centric coordinate systems necessary for the analysis. We then outline our subhalo selection criteria and track the LMC-associated subhalos, examining their spatial distribution and assessing their “faith”, i.e., whether they are bound to or disrupted by the LMC-analog or the MW.

Furthermore, we introduce our analytical model, outlining the assumptions used to compute stream–subhalo encounter rates. This involves integrating representative orbits for a suite of both synthetic and real MW streams to determine subhalo encounter rates.

2.1. Simulations

We select two cosmological zoomed-in baryonic simulations of MW-mass galaxies from the *Latte* suite (Wetzel et al. 2023) of the Feedback In Realistic Environments (FIRE) project.¹ These simulations are run with the FIRE-2 physics model (Hopkins et al. 2018) using the GIZMO code (Hopkins 2015) which utilizes a TREE+PM solver for gravity and a Lagrangian meshless-finite-mass (MFM) solver for hydrodynamics with adaptive spatial resolution. The FIRE-2 model implements star formation and stellar feedback parameters from the STARBURST99 stellar evolution models (Leitherer et al. 1999) in the Λ CDM cosmology from Planck (Collaboration et al. 2015). A detailed description of the FIRE-2 project can be found in Hopkins et al. (2018) and about the *Latte* suite of MW-mass systems specifically in Wetzel et al. (2016). Horta et al. (2023) made predictions for observable for LMC-analog accretion events in the *Latte* MW analogs while Panithanpaisal et al. (2021) studied mass distri-

¹ <http://fire.northwestern.edu/latte>

bution of massive stellar stream and their progenitors. Samuel et al. (2020) examined radial velocity distribution of satellites around isolated and paired MW–M31 analogs and showed that central disc tidally destroys satellites altering their radial profile. Samuel et al. (2021) showed that spatially thin MW-like planes of satellites can exist in cosmological simulation and presence of an LMC-analog increases the probability of such planes. Barry et al. (2023) did a statistical study of spherically average subhalo number density and estimated a boost of 1.2–2 due to LMC-analogs. They also estimated that a stream like GD-1 (Grillmair & Dionatos 2006) can have roughly 5–6 encounters per Gyr.

We select the two galaxies labeled m12i and m12b for our analysis. Both are similar to the MW in stellar and gas mass content as well as their DM mass and density profiles at the present day (Hopkins et al. 2018; Garrison-Kimmel et al. 2018; Sanderson et al. 2020). Each DM halo has a total mass of about $1. \times 10^{12} M_{\odot}$, and each simulation uses an initial particle mass of $m_b = 7100 M_{\odot}$ for stars and gas, and dark matter particle mass $m_{DM} = 35000 M_{\odot}$. m12b includes a massive satellite analogous to the LMC in the MW with its first pericentric passage about 5 Gyr before the present day, while m12i has a relatively quiescent history with no major mergers for the past 8 Gyr and is used as our “control” system.

We identify the LMC-analog in m12b based on the similarity of its orbit around first pericenter (Fig. 1), and on the similar merger mass ratio of about 1:8 at pericenter (Table 1). The orbit has $d_{\text{peri}} = 37.9$ kpc and $v_{\text{tot}} \approx 350$ km s⁻¹, comparable to the values of $d_{\text{peri}} = 49$ kpc and $v_{\text{tot}} = 350$ km s⁻¹ estimated for the LMC (Kallivayalil et al. 2006). Following Arora et al. (2022), we define the *total mass ratio* (TMR) to be the mass of the host galaxy divided by the mass of the satellite at T_{peri} and the *pericenter mass ratio* (PMR) to be the mass of the MW enclosed within d_{peri} divided by the mass brought in by the satellite within d_{peri} of the center of the satellite. The LMC-analog has a TMR of 7.3, while the estimated TMR for LMC is about $\sim 4 - 15$, assuming a MW mass of $1 - 1.5 \times 10^{12} M_{\odot}$ and LMC mass of $1 - 2.5 \times 10^{11} M_{\odot}$ (e.g. Peñarrubia et al. 2015; Vasiliev et al. 2021).

The main difference between our analog and the LMC, based on the models in Garavito-Camargo et al. (2019), is the plane of the satellite orbit relative to the hosts disk and that its first pericentric passage occurred about 5 Gyr before the present day. In our simulation, the LMC-analog’s orbit is inclined at 107° oriented with respect to the disk plane. However, we do not expect this difference to significantly impact our conclusions. This is because we are interested in computing subhalo stream interactions and determining their rates in different halo quadrants relative to the merger trajectory. Moreover, since the orientation of the LMC orbit and the orbit is not well-constrained due to uncertainties in measured positions and proper motion and in MW mass models (McMillan 2016; Pietrzyński et al. 2019), our simulation with a differently oriented LMC-analog provides a plausible scenario. The torque from the disk could affect the orientation and shape of the streams, but the effect is expected to be minor. In fact, a number of studies have investigated

the effect of the disk’s torque on the shape of tidal streams. For example, Law et al. (2005) found that the disk torque can significantly affect the orientation and shape of streams for nearly coplanar orbits, while for more inclined orbits the effect is much weaker. On the other hand, Kazantzidis et al. (2008) argued that the disk torque is generally not important for the formation of streams, since the subhalo motion in the host halo is dominated by the overall potential rather than the disk torque. Santistevan et al. (2023) showed that orbits of satellites in idealized host potentials are completely insensitive to host disk orientation. Furthermore, Garrison-Kimmel et al. (2017) showed that tidal disruption of subhalos remains largely unaffected by the geometry of the host disc. Therefore, while the effect of the disk torque on the shape of streams is still debated and likely depends on various factors such as the orbital parameters and the properties of the host and subhalo, it is generally believed to be small for orbits that are not nearly coplanar with the host disk.

The first pericenter passage of the LMC-analog in m12b occurs at a lookback time of about 5 Gyr (Table. 1) so we define the time T relative to it such that $T_{\text{peri}} = 0$ Gyr. The most massive perturber in m12i reaches the pericenter around the same time and is nearly an order of magnitude less massive relative to its host at the pericenter than the LMC-analog we identify in m12b. The age of our host galaxies at pericenter is thus less than the current age of the MW; however, given that the majority of star formation has slowed down by about 7 Gyr in both m12b and m12i (Hopkins et al. 2018) and the total mass of each halo is close to the MW at the time of the merger, we expect our simulations to be analogous to the real MW even though they are slightly younger than MW at satellite pericenter. Table. 1 summarizes the characteristics of the LMC-analog in m12b and the equivalent most massive satellite in m12i at $T_{\text{peri}} = 0$ Gyr.

Barry et al. (2023) showed that the presence of an LMC-analog can boost the subhalo number density by a factor of 1.2–2. They identified four LMC-analogs in simulations m12b, m12f, m12w, and m12c in FIRE-2 simulations, approximating properties when the analogs approach within 50 kpc of the center and not their actual pericentric distances. This method provides greater statistical accuracy when evaluating the contribution of LMC-analogs to the subhalo population, but not necessarily on subhalo phase-space distribution. Our focus here encompasses a global perspective that also considers the effects of the MW response to the in-falling satellites, which is dependent on the satellite’s orbit, actual pericenter distance, mass, and velocity. The LMC-analog orbit in m12f is similar to the orbit in m12b and expectations from the LMC, but the satellite is only half as massive, with a TMR of about 16 (Arora et al. 2022). Consequently, the host’s response to the LMC-analog in m12f is significantly weaker, possibly even negligible.

Moving on to m12w and m12c, both simulations feature satellites similar in mass to the LMC. However, m12w stands out due to its highly eccentric, fast-moving orbit, resulting in a very radial merger with its first pericenter at 8 kpc and eventual complete tidal disruption of the satellite. It’s almost

6.5 Gyr before the present day (1.5 Gyr earlier in comparison to m12b). This makes it highly unreliable for predictions. In contrast, the LMC-analog in m12c is closest to the present day but follows an orbit completely within the disc plane, with the actual first pericenter occurring at 18 kpc. This particular orbit is not expected to induce a north-south asymmetry. Selecting an arbitrary pericenter at 50 kpc would not accurately represent halo deformations. For the sake of completeness, we have included our encounter rates calculation for m12c in appendix .1.

2.2. Coordinates and frames for analysis

Introducing a second galaxy of non-negligible mass into the MW creates a proliferation of relevant coordinate systems that could be used for analysis, since we are now effectively considering a variation on the three-body problem. The MW-LMC system we consider involves two galaxies orbiting around their common center of mass (COM), which is moving with relatively constant velocity through space. The frame centered on and moving with the system COM is thus an inertial frame (modulo interactions with the next most massive satellite galaxy of the MW). We will refer to this as the **system frame**, related to the one in which the simulation is run (the “simulation box frame”) by a constant boost in velocity and a linear shift in position:

$$\vec{x}' = \vec{x}_{\text{sim}} - \vec{x}_{\text{sim}}^{\text{COM}}(t) \quad (1)$$

$$\vec{v}' = \vec{v}_{\text{sim}} - \vec{v}_{\text{sim}}^{\text{COM}} \quad (2)$$

where the subscript sim denotes quantities in the simulation box frame and the prime denotes quantities in the system frame; $\vec{v}_{\text{sim}}^{\text{COM}}$ is the constant velocity of the COM (so $\vec{x}_{\text{sim}}^{\text{COM}}(t) = \vec{v}_{\text{sim}}^{\text{COM}} \times t$ up to a constant).

From our perspective in the MW’s disk, however, the Sun orbits the center of the MW (the local minimum in the potential and maximum in density), and we commonly use a coordinate system centered on and moving with this location, referred to as the **Galactocentric frame**. This frame is not inertial, since the MW and LMC are orbiting their common COM, but instead is related to the system frame by:

$$\vec{x} = \vec{x}' - \vec{x}'_{\text{MW}}(t) \quad (3)$$

$$\vec{v} = \vec{v}' - \vec{v}'_{\text{MW}}(t) \quad (4)$$

where the unprimed quantities are in the Galactocentric frame, and \vec{x}'_{MW} and \vec{v}'_{MW} denote the position and velocity of the MW’s center in the system frame, both of which are functions of time (as explicitly highlighted in this equation). Since $d\vec{v}'_{\text{MW}}/dt \neq 0$, the Galactocentric frame is *not* inertial. The displacement of the Galactocentric frame in position and velocity is defined so that at the time of pericenter t_{peri} (the present configuration in the actual MW-LMC system):

$$\vec{x}(t_{\text{peri}}) = \vec{x}' - \vec{x}'_{\text{ref}} \quad (5)$$

$$\vec{v}(t_{\text{peri}}) = \vec{v}' - \vec{v}'_{\text{ref}}, \quad (6)$$

where \vec{x}'_{ref} is the distance between the MW center and the system COM, and \vec{v}'_{ref} is the relative motion of the MW’s

center induced by the LMC also known as the “reflex motion”, which for the real MW-LMC system is approximately 30-40 km s⁻¹ at the location of the Sun (Erkal et al. 2019; Petersen & Peñarrubia 2020; Vasiliev et al. 2021; Vasiliev 2023).

While in the standard analysis of subhalos used to interpret stream perturbations the system and Galactocentric frames are identical, this is not so in the MW-LMC system. Thus the choice of the right frame for analysis of stream–subhalo interactions depends on the location of the stream of interest relative to the LMC. Since the LMC is now interior to most of the MW’s halo, the Galactocentric frame is relevant for the disk and inner halo, where motion is dominated by the MW’s mass and takes place at shorter dynamical times than the orbit of the MW and LMC around their COM (represented by T_{sys}). The system frame is relevant for the outer halo, which feels the combined gravity of the MW-LMC system and evolves at longer dynamical times than T_{sys} . The transition between these two regimes occurs, naturally, at roughly the distance of the LMC.

Finally, to compute quantities relevant to stream–subhalo interactions the relevant frame is the one moving with the stream, here referred to as the **stream-centric frame**. Since most of the currently known streams are closer to the MW center than the LMC, we will relate the stream-centric frame, denoted by $\tilde{\vec{x}}$ and $\tilde{\vec{v}}$, to the Galactocentric frame \vec{x}, \vec{v} (for streams orbiting beyond the LMC one would substitute the system frame \vec{x}'):

$$\tilde{\vec{x}} = \vec{x} - \vec{x}_{\text{str}}(t) \quad (7)$$

$$\tilde{\vec{v}} = \vec{v} - \vec{v}_{\text{str}}(t), \quad (8)$$

where $\vec{x}_{\text{str}}(t), \vec{v}_{\text{str}}(t)$ are the position and velocity of a representative particle in the stream in Galactocentric coordinates (in other words, the stream’s representative orbit). The relevant quantity for determining the rate of subhalo interactions is the distribution of the radial velocities of subhalos in stream coordinates, \tilde{v}_r , given by

$$\tilde{v}_r = (\vec{v}_{\text{sub}} - \vec{v}_{\text{str}}) \cdot (\vec{x}_{\text{sub}} - \vec{x}_{\text{str}}) \quad (9)$$

where x_{sub} and v_{sub} denote the position and velocity of a subhalo in the Galactocentric frame. The relative positions of the stream and subhalo are identical in any frame, but the reflex velocity is a function of position. Unlike in the restricted three-body problem, the motion induced by the interaction with the LMC cannot be simply written as $\vec{\Omega} \times \vec{r}$, and it can be different for the stream in question than for the population of subhalos with which the stream interacts. We therefore simply express the relative velocity of the stream and subhalo as a function of their positions with respect to the MW-LMC barycenter, rather than adopting a particular functional form:

$$\tilde{v}_r = \left\{ \left[v_{\text{sub}} - v_{\text{ref}}(x_{\text{sub}}) \right] - \left[v_{\text{str}} - v_{\text{ref}}(x_{\text{str}}) \right] \right\} \cdot (x_{\text{sub}} - x_{\text{str}}) \quad (10)$$

Table 1. Properties of the most massive mergers in m12b (LMC-analog) and m12i.

Simulation	T_{peri} [Gyr]	redshift	$M_{\star, \text{host}}$ [$\times 10^{10} M_{\odot}$]	d_{peri} [kpc]	TMR	PMR	v_{rad} [km s^{-1}]	v_{tan} [km s^{-1}]
m12i	8.05	0.60	3.8	29.53	45.5	14.05	-13.4	290.2
m12b	8.81	0.49	6.3	37.9	8	3	-9.7	349.2

NOTE— T_{peri} : Time of closest approach (“pericenter”) between the main galaxy and the satellite ($T = 0$ Gyr). All properties are evaluated at T_{peri} . $M_{\star, \text{host}}$: Stellar mass of the halo. d_{peri} : Pericenter distance between satellite and main galaxy. TMR: Total Mass Ratio of the MW and the satellite, $M_{\text{main}}/M_{\text{sat}}$, and PMR: Pericenter Mass Ratio, $M_{\text{main}}(< d_{\text{peri}})/M_{\text{sat}}(< d_{\text{peri}} \text{ from sat})$. v_{rad} , v_{tan} : radial and tangential velocities of the satellite with respect to the MW. v_{rad} is non-zero due to finite time resolution between snapshots around the pericentric passage.

Table 2. Quadrant cutoffs in Sky coordinates.

Quadrant	No.	ϕ ($^{\circ}$)	θ ($^{\circ}$)
North-East	I	-180 – 0	0 – 90
North-West	II	0 – 180	0 – 90
South-West	III	0 – 180	-90 – 0
South-East	IV	-180 – 0	-90 – 0

NOTE—where ϕ and θ correspond with azimuth and altitude respectively in mollweide projection. Refer to Fig. 6 b.) for a visual representation.

Since, x_{sub} and x_{str} are relatively close, we can expand $v_{\text{ref}}(x_{\text{sub}})$ using a first-order Taylor expansion around $v_{\text{ref}}(x_{\text{str}})$. This allows us to approximate Eq. 10 as:

$$\tilde{v}_{\text{r}} \approx (v_{\text{sub}} - v_{\text{str}}) \cdot (x_{\text{sub}} - x_{\text{str}}) - \left[x_{\text{sub}} - x_{\text{str}} \right]^{\text{T}} \frac{\partial v_{\text{ref}}}{\partial \vec{x}} \Big|_{x_{\text{str}}} \left[x_{\text{sub}} - x_{\text{str}} \right] \quad (11)$$

where $\frac{\partial v_{\text{ref}}}{\partial \vec{x}} \Big|_{x_{\text{str}}}$ is the velocity distortion matrix, which can be decomposed into symmetric and anti-symmetric components. When computing the mean $\langle v_{\text{rad}} \rangle$, only the anti-symmetric part or “shear” in velocity distortion will contribute to the average. Therefore, asymmetry in the velocity distortion around a stream leads to a non-zero $\langle v_{\text{rad}} \rangle$, as is expected in the velocity field of the MW–LMC system (Cunningham et al. 2020; Petersen & Peñarrubia 2020).

Fig. 1 plots the trajectory of the LMC-analog (red/green) in m12b in Galactocentric coordinates along with the total distance from the MW’s central location (on the bottom right) compared to a MW-LMC constrained simulation (blue) from Garavito-Camargo et al. (2019).

We will compute subhalos-stream encounter rates in four quadrants in the sky. We define each quadrant in Galactocentric coordinates in Table. 2 for future reference, also marked in Fig. 1 YZ panel.

2.3. Subhalo selection

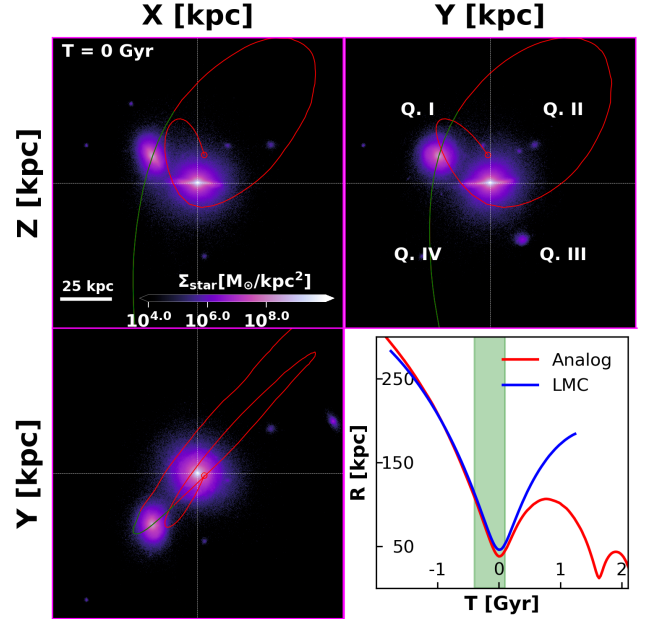


Figure 1. Trajectory of the LMC-analog (red/green) in Galactocentric coordinates from FIRE-2 simulation of a MW-mass galaxy labeled m12b with stellar surface density in the background, such that the disc is in the XY plane at $T = 0$ Gyr (1st pericenter). Quadrant labels based on Table. 2 are marked in YZ plane. Bottom right: the distance from the galactic center as a function of time for the FIRE analog (red/green), compared to the MW-LMC simulation 3 from (Garavito-Camargo et al. 2019) (blue). The analog orbit is in green between -0.4 to 0.1 Gyr.

We use the ROCKSTAR halo finder (Behroozi et al. 2012a) to identify DM subhalos. Merger trees were constructed to link the catalogs at each snapshot using the `consistent-trees` code (Behroozi et al. 2012b), as detailed in Samuel et al. (2021) and Panithanpaisal et al. (2021). Using these halo catalogs we identify subhalos that are brought in by the LMC-analog. We select subhalos between the mass range of $10^6 M_{\odot} \leq M_{\text{sub}} \leq 10^9 M_{\odot}$ and bound to and within the virial radius of the LMC-analog 2 Gyr before the first pericenter; when the d_{LMC} is greater than the virial radius of MW, and track their evolution through time until disruption

using `consistent-trees`. We impose the same mass selection criteria on the MW subhalos when computing the subhalo-stream interaction rates. The LMC-analog has a total of 1029 subhalos. Fig. 2 plots the location of LMC-analog subhalos as density contours in the XZ plane for m12b at -1 Gyr (left), 0 Gyr (middle), and 1 Gyr (right) with the LMC-analog trajectory and location (shown in red). Insets on the top left plot the stellar density in the same plane, while insets on top right shows the density of these subhalos in mollweide projection. The LMC-analog starts in the south and falls toward the galactic center bringing it's own population of subhalos that are widely distributed in different regions and settle into newer bound orbits around the MW as this merger proceeds. Note the trailing subhalos behind the satellite at pericenter in both Cartesian plane and mollweide projection. Similar LMC subhalo distributions with leading and trailing arms are noted in Sales et al. (2017).

We track whether these subhalos are bound to satellite or the host using a total negative energy criteria (i.e $E_{\text{sub,tot}} \leq 0$ in satellite or host reference frame). We quantify whether the subhalos merged into the satellite or the host. A subhalo is considered “merged” when `consistent-trees` can no longer track it's center and it's descendant subhalo links to either the MW host or the in-falling satellite. `consistent-trees` can successfully track subhalos with masses greater than $10^6 M_{\odot}$.

Fig. 3 illustrates the number of LMC-analog subhalos bound to analog (blue) or the MW (orange), merged into the analog (green) or the MW (red) as a function of time starting from 2 Gyr before the first pericenter passage. By the first pericenter (0 Gyr), the majority of the subhalos are tidally stripped from the satellite and bound to the MW. By 1 Gyr, 90% of the subhalos from the satellite get tidally stripped and only half of the subhalos survive the merger while the rest are destroyed and form dark streams. In the scope of our simulations and our inability to resolve these dark streams, we leave them out of our calculations for future research. These dark streams are less likely leave observable signatures after their interactions with stellar streams because of their low surface density.

2.4. Analytic treatment of Encounter rates

We calculate the encounter rate at each snapshot of our simulation between subhalos and a stellar stream using the counting scheme described by Erkal et al. (2016), which is similar to the work conducted by Yoon et al. (2011). We consider the number of subhalos entering a cylinder of radius b_{max} (impact parameter) around a straight line stream of length ℓ_s . The rate depends on the local number density of subhalos n_{sub} around the stream and cylindrical radial velocity \tilde{v}_r distribution of subhalos with respect to the stream. We assume the radial velocity distribution to be Gaussian with mean $\tilde{\mu}$ and velocity dispersion $\tilde{\sigma}$. This is a departure from Erkal et al. (2016), where they assumed $\tilde{\mu} = 0$ for the radial velocity distribution. However, as discussed above, the dynamical disequilibrium caused by a massive-infalling satellite can create a non-zero $\tilde{\mu}$.

The number of subhalos passing through a cylinder of length ℓ_s and radius b_{max} at time t_{snap} , within a time interval dt , is then given by

$$dN_{\text{enc}}(t_{\text{snap}}) = (2\pi b_{\text{max}} \ell_s) \cdot (|\tilde{v}_r| dt) \cdot n_{\text{sub}} \cdot P(\tilde{v}_r | \tilde{\mu}, \tilde{\sigma}) d\tilde{v}_r \quad (12)$$

Here, $P(\tilde{v}_r | \tilde{\mu}, \tilde{\sigma})$ represents the Gaussian distribution of the radial velocity of subhalos in stream-centric coordinates with a non-zero $\tilde{\mu}$ and dispersion $\tilde{\sigma}$. In Appendix .2, we demonstrate that Gaussian distributions serve as reasonable approximations for $P(\tilde{v}_r | \tilde{\mu}, \tilde{\sigma})$. In this calculation, we consider only subhalos entering through the sides of the cylinder, so we integrate over all negative radial velocities (i.e. subhalos moving toward the stream). The resulting encounter rate then becomes

$$\frac{dN_{\text{enc}}}{dt}(t_{\text{snap}}) = \sqrt{2\pi} \tilde{\sigma} b_{\text{max}} \ell_s n_{\text{sub}} \cdot f(\tilde{\gamma}) \quad (13)$$

where, $f(\tilde{\gamma}) \equiv e^{-\tilde{\gamma}^2} + \sqrt{\pi} \tilde{\gamma} (\text{erf}(\tilde{\gamma}) - 1)$,

where $\tilde{\gamma} \equiv \frac{\tilde{\mu}}{\sqrt{2}\tilde{\sigma}}$. $f(\tilde{\gamma})$ is a scaling factor that depends on the mean subhalo radial velocity. This factor equals unity when $\tilde{\mu} = 0$ for the traditional encounter rate formulation such as in Yoon et al. (2011); Erkal et al. (2016); Barry et al. (2023). Fig. 4 plots $f(\tilde{\gamma})$ as a function of $\tilde{\gamma}$. The scaling factor approaches 0 for a large positive mean velocity (i.e. all the subhalos directed away from the stream) and diverges to infinity for a large negative mean velocity (all the subhalos headed straight for the stream). For a typical velocity dispersion in the outer halo $\sigma = 100 \text{ km s}^{-1}$ (Deason et al. 2012; Cohen et al. 2017) and expected shift of $\tilde{\mu} = 35 \text{ km s}^{-1}$ (Erkal et al. 2019; Petersen & Peñarrubia 2020) for a stream in a circular orbit, $f(\tilde{\gamma})$ will scale the encounter rates to 1.75 or 0.5 depending on whether $\tilde{\mu}$ is locally negative or positive in the stream's frame. Notably, a negative $\tilde{\mu}$ value leads to more substantial rate enhancements than a positive $\tilde{\mu}$ leads to reductions. For instance, a $\tilde{\gamma}$ of -0.25 results in a 50% boost in encounter rates, while a +0.25 value leads to a 35% decrease. Likewise, a +0.5 value corresponds to a 64% decrease, whereas a -0.5 value leads to a 112% enhancement. For halos with no massive satellites, Barry et al. (2023) showed that in galactocentric frame at present day, the orbital velocity vectors of subhalos are generally isotropic at all distances.

To evaluate Eq. (13) in our simulations, we compute an average n_{sub} as a function of time, by counting the number of subhalos within a 10 kpc width spherical shell around a stream in its respective quadrant at each time step and dividing by the volume of the shell. Similarly, we compute $\tilde{\mu}$ and $\tilde{\sigma}$ by calculating the mean and standard deviation of the radial velocities of subhalos, in stream-centric coordinates, within the same shell, and in stream's quadrant for each time step of the stream. In our framework, we calculate the encounter rate at each snapshot using Eq. 13, and we sum the number of encounter per Gyr for a stream using the equation:

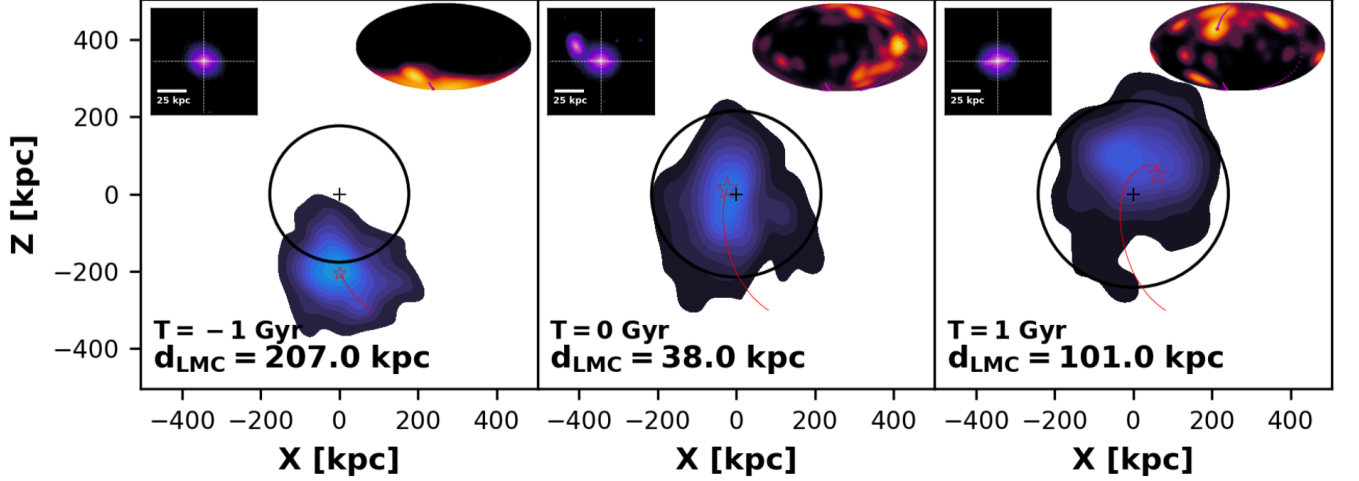


Figure 2. Density contours of surviving subhalos brought in by the LMC-analog at three time steps: -1 Gyr (left), 0 Gyr (middle), and 1 Gyr (right) along with the LMC trajectory (red) in XZ plane for m12b. The black circle marks the virial radius of the MW, while the top left inset plots the zoomed-in stellar density, and the top right inset shows the LMC subhalo density in mollweide projection at each time step. As the LMC falls in the MW, LMC subhalos are tidally stripped away from it and settle into bound orbits around the MW. This is obvious at 0 and 1 Gyr, as the density contours are more widespread in both cases. At 0 Gyr, Majority of the LMC subhalos lag behind the in-falling satellite and some are completely settled into new orbits producing a dipole term in density. At 1 Gyr, almost all of the subhalos are dispersed away from the LMC, as the central density of subhalos is far away from the satellite. Also note, there is slingshot action as a few subhalos end up unbound and outside the virial radius of the MW after LMC’s flyby (top right corner for $T = 1$ Gyr).

$$\frac{N_{\text{enc}}}{\text{Gyr}} = \frac{\sum_{t_{\text{snap}}} \frac{dN_{\text{enc}}}{dt}(t_{\text{snap}}) \Delta t_{\text{snap}}}{\sum_{t_{\text{snap}}} \Delta t_{\text{snap}}}. \quad (14)$$

Here, Δt_{snap} represents the time interval between snapshots, and the sums are taken over all time steps t_{snap} .

2.5. Integrating stellar stream orbits

For our analytic model to compute stream–subhalo encounter rates, we represent each stream as a test particle with a fixed length of $\ell_s = 10$ kpc and impact parameter $b_{\text{max}} = 1$ kpc. We report the number of encounters per Gyr per 10 kpc per b_{max} as $\frac{N_{\text{enc}}}{\text{Gyr}}$. We suppress the implicit dependence on impact parameter and stream length (and the details of the stream’s structure) in order to compare encounter rates in different regions on the sky, with explicit dependence on n_{sub} and $\tilde{\gamma}$.

We integrate orbits for two kinds of streams in our halos to probe the dependence of the encounter rate on location relative to the LMC analog:

- **MW streams:** 97 distinct streams orbiting the MW with phase-space properties in Galactocentric coordinates derived from *galstreams* (Mateu 2023) rotated to match the orientation with the LMC-analog in m12b. We take the median phase-space value from the stream track to compute stream-centric coordinates and assume a $\ell_s = 10$ kpc. We start integration for each stream at $T = 0$ Gyr.
- **Synthetic streams:** 5000 synthetic streams as point particles with fixed length $\ell_s = 10$ kpc at varying lo-

cations in the sky and different orbital properties. We simulate these streams to be at their pericenter with distances between 20-80 kpc from the galactic center at $T = 0$ Gyr, spread uniformly across the sky in a Mollweide projection, and varying azimuthal velocities and inclination velocities such that the total tangential velocities at $T = 0$ Gyr are between 250-400 km s⁻¹ (set by real MW streams). These initial condition produce a uniform distribution of streams’ orbital eccentricities and pericentric distance in all quadrants.

For MW streams, we employ the median position and velocity of each stream track in Galactocentric coordinates as our initial condition. While each stream is still represented as a test particle, we modify the initial condition by rotating the stream’s position such that its alignment with the LMC-analog in m12b is the same as its alignment with the real LMC. To achieve this, we utilize a rotation matrix R_{LMC} , computed using Rodrigues’s rotation formula, which aligns the real LMC position unit vector (\hat{x}_{LMC}) with the LMC-analog’s unit vector (\hat{x}_{analog}) in m12b such that $\hat{x}_{\text{analog}} = R_{\text{LMC}}^T \hat{x}_{\text{LMC}}$:

$$R_{\text{LMC}} = I + [v]_{\times} + \frac{[v]_{\times}^2}{1 + \hat{x}_{\text{LMC}} \cdot \hat{x}_{\text{analog}}} \quad (15)$$

where I is the identity, v is given by $\hat{x}_{\text{LMC}} \times \hat{x}_{\text{analog}}$, and $[v]_{\times}$ is the skew symmetric cross-product of v . We apply this rotation to the median phase-space coordinates of the MW stream, aligning its orientation with that of real streams relative to the real LMC within our framework.

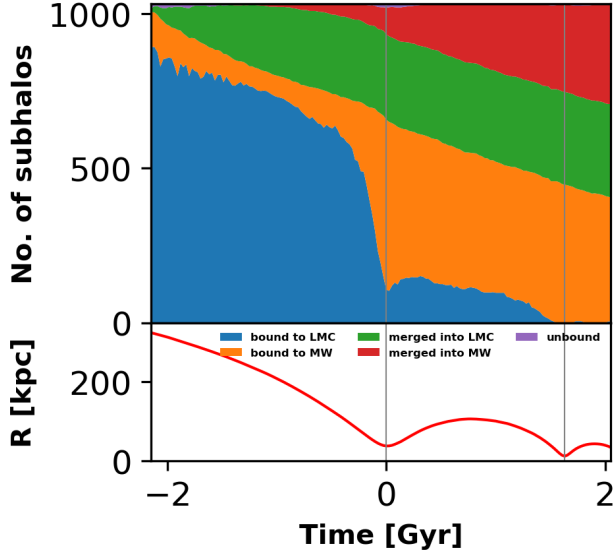


Figure 3. The bound properties of 1029 LMC-analog subhalos with mass range $10^6 M_{\odot} \leq M_{\text{sub}} \leq 10^9 M_{\odot}$ at different time steps to illustrate whether they are still bound to the LMC-analog (blue), bound to the MW (orange) or merged into the MW (red) or the LMC-analog (green). The number of subhalos bound to the analog drastically drops after the first pericentric passage where the tidal forces from the MW are stronger and hence they become bound to the MW. By the second pericenter passage, most of the subhalos are either bound to the MW or have been completely tidally stripped by the LMC-analog or the MW. Only about 50% subhalos survive after the merger is complete. The number of subhalos brought by the LMC-analog that merged into it (green) increases as the the analog gets closer to the MW but remains constant after the first pericenter. While more subhalos merge into the MW (red) as the merger proceeds. Note the few unbound subhalos at 0 Gyr are due to instability of any potential model to accurately describe the MW–LMC system.

For the specific values of $\vec{x}_{\text{LMC}} = (-1, -41, -28)$ kpc and the analog in m12b $\vec{x}_{\text{analog}} = (-23, -27, 14)$ kpc, the rotation matrix is given by:

$$R_{\text{LMC}} = \begin{pmatrix} 0.7447286 & 0.30812051 & 0.59198063 \\ -0.65937004 & 0.47663041 & 0.58142463 \\ -0.10300712 & -0.82333784 & 0.55812573 \end{pmatrix} \quad (16)$$

To integrate the orbits of the test particles (each representing a stream), we use time-evolving potential models from Arora et al. (2022), fitted with basis function expansions (BFEs) on the host halo in each snapshot in a window around $T = 0$. These models capture the large-scale deformation of the mass distribution by the LMC. Since we represent each stream by the orbit of a single test particle, the torque on this parent orbit is accounted for by our integration, but the relative torque on leading and trailing arms of the stream (as is observed, for

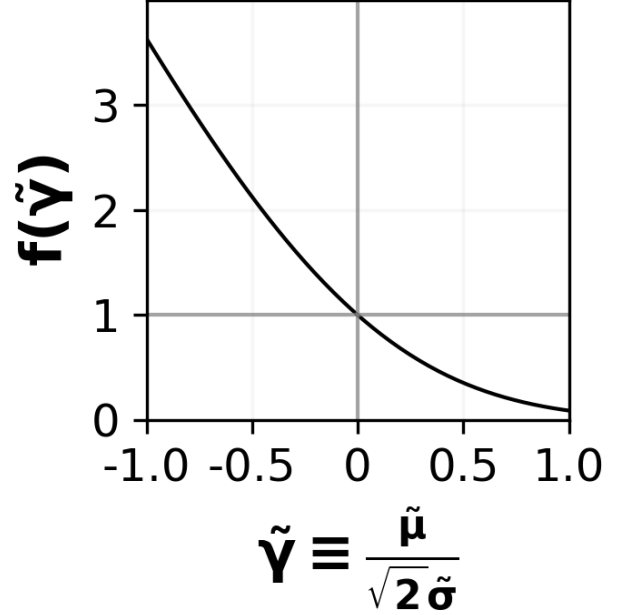


Figure 4. The scaling factor $f(\tilde{\gamma})$ in Eq. 13 that is dependent on the Gaussian parameters of the radial velocity distribution of subhalos w.r.t a stream as a function of typical $\tilde{\gamma}$, i.e is function of mean radial velocity ($\tilde{\mu}$) and velocity dispersion ($\tilde{\sigma}$) of subhalos in stream-centric coordinates. Theoretically the factor converges to 0 with $\tilde{\gamma} \gg 0$ and diverges to infinity for $\tilde{\gamma} \ll 0$. $f(\tilde{\gamma})$ strongly depends upon $\tilde{\mu}$ and $\tilde{\sigma}$ and hence assuming $\tilde{\mu} = 0$ can bias estimates of encounter rates.

example, in the real-life Orphan stream (Lilleengen et al. 2023)) is not captured.

We integrate the stream orbits within a time span of -0.4 to 0.1 Gyr, which corresponds to approximately 20 snapshots (marked by green in Fig. 1). The time range is selected to maximize perturbations caused by the LMC-analog, considering that the actual LMC had its first pericenter passage roughly 60–100 Myr ago (Besla et al. 2007; Vasiliev 2023). Furthermore, the integration duration of 0.5 Gyr is sufficient to induce noticeable morphological changes in a stream’s structure, such as the emergence of open gaps and the occurrence of kinks (Erkal & Belokurov 2015b). While our orbit integration of subhalos and streams is not entirely self-consistent, as the subhalos respond to the LMC-analog in a live simulation while the streams are integrated within a smooth, time-evolving potential, BFEs can adequately describe deformations in the halo caused by LMC-analogs (e.g Petersen & Peñarrubia 2020; Garavito-Camargo et al. 2021; Petersen et al. 2022; Arora et al. 2022). BFEs have also been shown to successfully reproduce orbits, even in the presence of massive satellites, for short periods of time (less than 1 Gyr) in both idealized simulations (Lilleengen et al. 2023; Vasiliev 2023), and cosmological simulations (Lowing et al. 2011; Sanders et al. 2020; Arora et al. 2022).

We use the integrated orbits to calculate apocenter and pericenter distances, and categorize streams as prograde or

retrograde relative to the orbit of the LMC analog in m12b. Only about 13 of the known MW streams have pericenter distances greater than 20 kpc from the galactic center in the m12b potential.

3. EFFECTS OF MASSIVE SATELLITES ON ENCOUNTER RATES

The encounter rates, as defined in Eq. 13, depend on two crucial parameters: $f(\tilde{\gamma})$ and n_{sub} . Under the standard assumptions of isotropy and spherical symmetry, n_{sub} has no angular dependence and falls off with radius, while $f(\tilde{\gamma})$ is assumed to be unity, indicating a Gaussian distribution of subhalos' radial velocities in stream-centric coordinates centered around zero with a constant dispersion. However, when a massive satellite such as the LMC falls into the MW, both of these parameters experience perturbations that vary across different locations relative to the present position of the LMC and its orbit around the MW. In this section, we quantitatively analyze the azimuthal changes in number density and Gaussian parameter resulting from the infall of an LMC-analog.

3.1. Phase-space distribution of the perturbed subhalo population

We begin by characterizing the phase-space distribution of both the host subhalos (those bound to the MW and not brought in by the LMC-analog) and the subhalos brought in by the LMC-analog, here after *contributed* subhalos, as a function of time, to demonstrate how the presence of contributed subhalos influences the overall distribution and dynamics of subhalos within the system.

Fig. 5 shows this distribution at three equally spaced time steps 1 Gyr before pericenter (left column), when the LMC-analog is at pericenter (center column), and 1 Gyr after pericenter (right column).

The ratio of contributed subhalos to total subhalos as a function of radius is plotted in the top row. Despite the contributed subhalos comprising only a small fraction (less than 10%) of the host subhalos, they can increase the spherically averaged subhalo density near the LMC-analog's radial distance (indicated by the red dashed line) by up to 20%. Barry et al. (2023) noted higher boosts from LMC-analogs, m12b in their analysis has one of the lower boost factors, in part because it occurs earlier, when the overall number of subhalos in the MW halo was higher. Therefore, our boosts of 20% from LMC-analog contributed subhalos serves as a lower limit for FIRE-2 simulations.

The middle and bottom rows show the total and radial velocity distributions in Galactocentric coordinates of contributed subhalos (depicted as open contours) respectively, relative to the background MW subhalo distribution (depicted as filled contours) within the virial radius. It's important to highlight that the LMC-analog's position isn't centered within the open contour distribution. This is a result of focusing solely on subhalos situated within the MW's virial radius, which doesn't encompass the densest region of the contributed subhalos. Notably, at $T = -1$ Gyr, both the total and radial velocity distributions reveal a distinct leading arm (higher density closer

to the host center) of contributed subhalos compared to the in-falling satellite (indicated by the red star). The trailing arm of contributed subhalos is mostly outside of the virial radius.

Furthermore, the overall distribution of contributed subhalos within the virial radius exhibits unique characteristics compared to the MW. At $T = -1$ Gyr, the mean radial velocity of the contributed subhalos is shifted by approximately 150 km s^{-1} (marked by the dashed red line), corresponding to the satellite's radial velocity. By $T = 0$ Gyr, the mean radial velocity of the surviving contributed subhalos aligns within $\pm 25 \text{ km s}^{-1}$ of the host population as the populations of contributed subhalos is not fully phase-mixed. As the merger progresses, the surviving subhalos gradually phase-mix into new orbits resembling those of the MW background subhalos, evident as early as 1 Gyr after the first pericentric passage, consistent with the analyses in Sales et al. (2017) and Barry et al. (2023). Note that the tangential velocity distribution of subhalos in Galactocentric coordinates show similar trends as the total velocity distribution in middle row.

The escape velocity curves are overlaid in the middle row at each time step. While the majority of subhalos lie below the escape velocity, some exhibit higher total velocities. However, many of these subhalos are falling towards the galactic center and thus experience stronger tidal stripping. The insets in the top right corner of the middle row provide a visualization of the mass distribution of the contributed subhalos within the virial radius.

In summary, the presence of contributed subhalos can increase the spherically averaged subhalo density by up to 20-40% (appendix .1), Barry et al. (2023) notes a higher boost due to contributed subhalos from other LMC-analogs. This effect will become more pronounced when considering the azimuthal dependence of subhalo density. Surviving contributed subhalos gradually phase-mix into new orbits resembling background subhalos. However, before $T = 0$ Gyr, they can shift the mean radial velocity of subhalos, influencing the Gaussian parameters and stream-subhalo encounter rates (Eq. 13). These effects are most prominent during the first pericenter passage and can either increase or decrease the encounter rates.

3.2. Quantifying the host's reflex motion with the total subhalo population

The local subhalo density and velocity distributions are not only affected by the contribution of additional subhalos from the LMC-analog. They are also perturbed by the shift of the COM frame induced by the presence of a massive satellite, which modifies $f(\gamma)$ and n_{sub} as discussed in Sec. 2.2. Here we consider the size of these effects in our simulated MW-LMC analog.

In Fig. 6 a.), we present the total central velocity of the MW's central position over time for both m12b (blue) and m12i (green). The MW central position is determined using the center-of-mass of stars and iteratively shrinking the sphere to achieve a consistent location (Power et al. 2003). The total central velocity is calculated based on the mean velocities of stars within 10 kpc of the MW center.

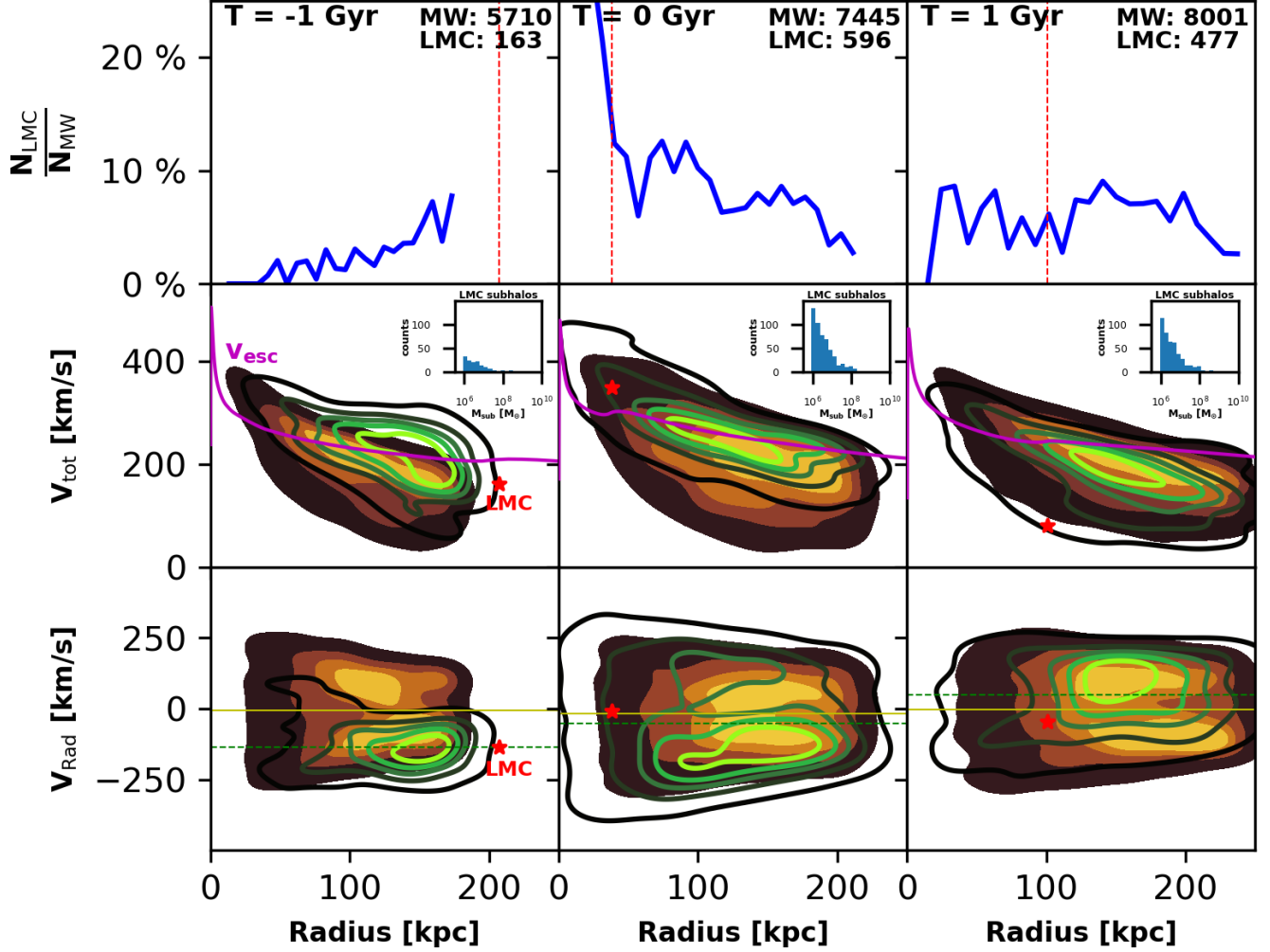


Figure 5. Phase-space evolution of MW-analog subhalos and LMC-analog contributed subhalos within the MW-analog's virial radius. Each column shows the distributions at different times: -1 Gyr (left), 0 Gyr (center), and 1 Gyr (right). Top row: fraction of contributed subhalos as a function of distance. Only a small fraction of subhalos (less than 10%) are brought in by the LMC-analog, yet they induce significant changes (around 20%) in the spherically averaged subhalo number density near $T = 0$ Gyr, especially around the LMC-analog's pericentric distance. The red dashed line shows the location of LMC-analog in each snapshot. Middle: distribution of total velocity in Galactocentric coordinates versus radius for the MW background (filled contours) and contributed (open contours) subhalos, along with the host's escape velocity curve (magenta) at each time. Insets show mass distribution of contributed subhalos. Tangential velocity of subhalos in Galactocentric coordinates show similar trends to total velocity. Bottom: radial velocity in Galactocentric coordinates versus radius for both subhalo populations. The mean radial velocity in Galactocentric coordinates of MW subhalos and contributed subhalos is marked by solid yellow and dashed green lines respectively. The red star marks LMC-analog's location. Both the phase-spaces stabilize after the first pericenter. By $T = 1$ Gyr, the contributed subhalos distribution matches the MW background as the subhalos undergo phase-mixing.

As the LMC-analog approaches its first pericentric passage, there is a significant change in the host's mean velocity. This change is primarily caused by the massive satellite in m12b shifting the center of mass of the system away from the host's center. This persists for 1–1.5 Gyr after the first pericenter as the LMC and MW analogs orbit their common COM. The effect reaches another peak as the system approaches its second pericenter passage at approximately 1.7 Gyr. In contrast, no such effects are observed in m12i which has a relatively constant velocity of about 130 km s^{-1} in time with

kinematical deviations of order 10 km s^{-1} in consistency with the results from Salomon et al. (2023).

In Fig. 6 b.), we present the direction of unit vectors \mathbf{v}_{host} of the host with respect to its present-day \mathbf{v}_{host} in spherical coordinates (indicated by triangle markers). We also show the trajectory of the LMC-analog (represented by a solid circle marker) as a function of time (color bar) for m12b. Each point on the plot indicates the direction and magnitude of the net velocity of the host. The distance of a marker from the origin reflects the strength of the centers' displacement and hence the

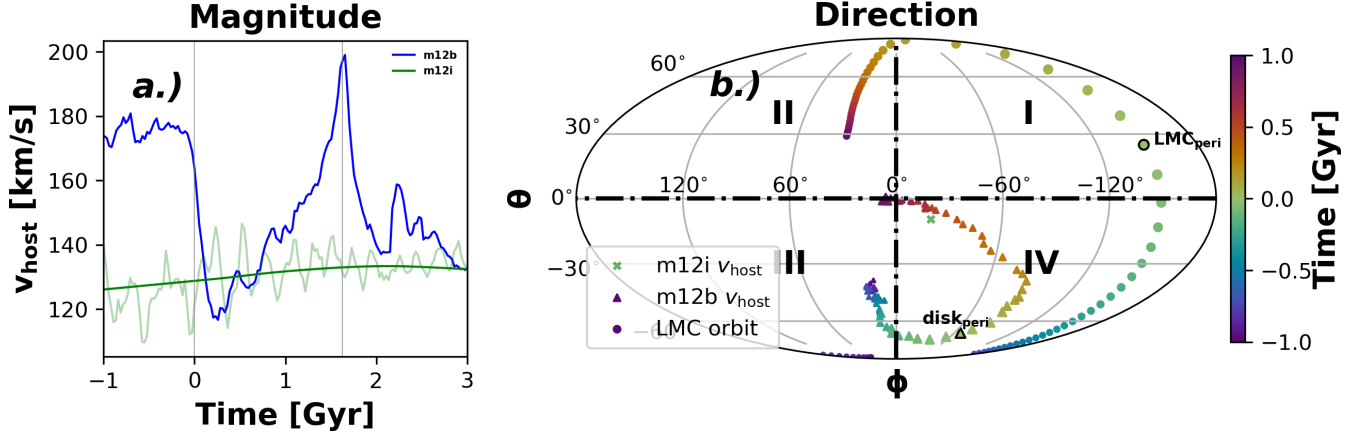


Figure 6. a.) Total central velocity of the main halo in m12b (blue) and m12i (green) as a function of time computed using shrinking spheres (Power et al. 2003). The sudden change in the host velocity is evident as the LMC-analog passes its first pericenter position at $T = 0$ Gyr (indicated by gray line), leading to another spike at $T = 1.6$ Gyr (the second pericenter passage). Eventually, the effect stabilizes as the LMC-analog undergoes tidal stripping in the MW potential. No such changes are noted in m12i, the isolated halo without massive satellites. b.) The unit vector of relative central velocity in spherical coordinates (triangle) quantifying the response to in-falling LMC-analog (circle) for m12b as a function of time (color bar). Each marker indicates both the direction and magnitude of the response, with markers further away from the origin indicating a stronger response. A clear systematic trend is observed, showing the MW center aligning with the direction of the LMC-analog, with the maximum magnitude occurring at $T = 0$ Gyr. The size of markers are relative to proximity of LMC-analog to the MW center. On the other hand, no distinct trends are observed for m12i. The average direction of MW center response is marked with a green cross for m12i.

reflex motion on positional velocities. Additionally, the size of the markers is inversely proportional to the galactocentric distance of the LMC-analog.

As the LMC-analog transitions from the Q.III to the Q.IV and moves closer to the galactic center, the MW center shifts towards the trajectory of the LMC-analog. This effect is most pronounced when the LMC-analog approaches its first pericenter at $T = 0$ Gyr. By the time of the LMC-analog’s second pericenter, the induced reflex motion is not as strong as the halo starts to relax and the satellite loses energy. In contrast, m12i does not show a systematic trend with the merging satellite and exhibits a randomly distributed velocity vectors. The green cross marker represents the average central displacement over the duration of the satellite merger. The reflex motion can perturb the mean of Gaussian velocity distribution, leading to changes in γ , which is a crucial factor in the calculation of encounter rates.

In Fig. 7 we plot the mean radial velocity of subhalos in Galactocentric coordinates $\langle v_{\text{rad}} \rangle$ in multiple 20 kpc radial bins to quantify how the MW center displacement affects stream-subhalo encounter rates. We observe a drop of a factor of 2 at the LMC-analog’s first pericenter in m12b for all subhalos within the virial radius (solid black). This negative drop can be attributed to the overall motion of subhalos directed towards the COM of MW-LMC system, as well as the local distribution of the contributed subhalo population with its own distinct phase-space properties. Similarly, the mean tangential velocity of subhalos in Galactocentric coordinates also changes by about 30 km s^{-1} .

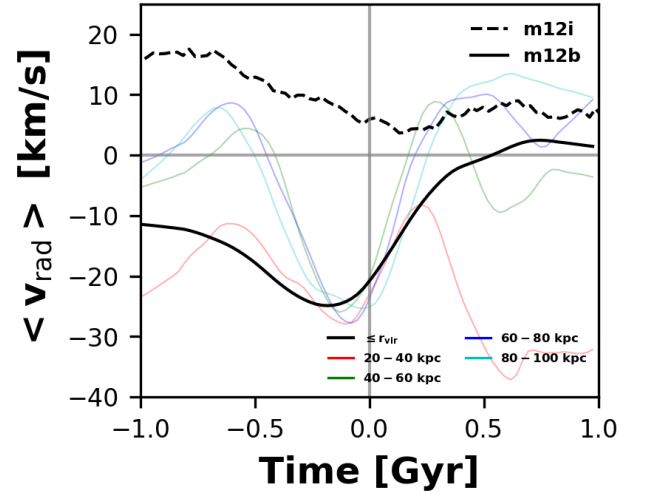


Figure 7. The mean radial velocity of all subhalos in Galactocentric coordinates for m12b (solid lines) and m12i (black dashed line) as a function of time, with different radial bins color-coded. The data are smoothed using the *loess* smoothing method (Cleveland & Devlin 1988). The mean radial velocity undergoes significant changes in m12b as the LMC-analog approaches its first pericenter passage. However, the radial velocity stabilizes again as the LMC-analog undergoes tidal stripping. In contrast, m12i exhibits a relatively constant mean radial velocity throughout the time-frame (computed within r_{vir}).

The changes in the mean radial velocity across different radial bins (represented by colored solid lines) exhibit similar trends, showing a distinct drop at $T = 0$ Gyr. The most significant deviations are observed in the 40–60 kpc bin (solid green) and the 60–80 kpc bin (solid blue), corresponding to the distances probed by the LMC-analog during the given time interval. The high magnitude and variation in 20–40 kpc bin is attributed to small number statistics. m12i (dashed line) demonstrates a relatively low and constant mean value.

3.3. distance and azimuthal dependence of μ and σ

Two major perturbations significantly affect the radial velocity distribution: the addition of contributed subhalos with different radial velocity distributions from the host, and the reflex motion, which is dependent on location and distance. To simplify the analysis, we utilize quadrants as proxies for angular dependence.

In Fig. 8, we quantitatively assess these two effects in Galactocentric coordinates by evaluating the change in $f(\gamma)$ Eq. 13. Specifically, we calculate $[f(\gamma) - f(0)] \times 100$ to determine the percentage change from the assumption of $\mu = 0$ in all quadrants. We consider three different 20 kpc intervals between 20–80 kpc for m12b with contributed subhalos (labeled as m12b, dark blue) and w/o contributed subhalos (labeled as m12b (no LMC), light blue), as well as for m12i (green). Note, these calculations can act as proxies for streams in a fully circular orbit at the center of each distance bin in the respective quadrants. The regions with a localized influx of contributed subhalos are marked with red boxes in the respective quadrant and distance range panels, and we track the presence of the LMC-analog in a quadrant and respective distance bin at a time with a magenta bar on the top of each panel.

When comparing the changes in $f(\gamma)$ between m12b with and without contributed subhalos, we observe that as the analog approaches its first pericenter, the m12b trends are consistently higher than m12b (no LMC) by approximately 20% in Q.IV. Both m12b systems show a positive increase trend as the analog moves closer to the center, while m12i exhibits oscillations ranging between $\pm 20\%$. As the contributed subhalos begin to experience tidal stripping, the trends in both m12b converge at around 0.1 Gyr after the first pericenter as these subhalos settle into new orbits around the MW, resulting in diminishing effects on the radial velocity parameters.

The reflex motion effect is most pronounced in the direction opposite to the line of sight of the MW-LMC vector. We mark these regions with purple boxes, which are polar opposite to the LMC-analog trajectory. The magnitude of this effect depends on the distance bin, as the inner and outer halos respond differently to the satellite perturbation, as well as on the analog’s orbital and tidal disruption properties. From approximately -0.5 to 0 Gyr, we observe this effect in Q. II. However, it becomes dominant only when the analog is very close to its first pericenter, where the encounter rates can change by as much as -25% to $+75\%$. At pericenter, as the analog transitions from Q. IV to Q. I, reflex motion perturbations briefly affect Q. III before the analog moves

past to Q. II and further away from the galactic center. This perturbation subsides as the velocity displacement of the MW center aligns back with the angular momentum axis of the disk. As the analog approaches its second pericenter, where 90% of the satellite’s mass has been stripped, the reflex motion effects become less significant.

In the case of m12i (green), the change in $f(\gamma)$ remains within $\pm 20\%$ for distances greater than 40 kpc, unless there is a massive satellite orbiting the main galaxy. Fluctuations are visible in the 20–40 kpc distance bin, but they are primarily due to low number statistics.

3.4. Impact on the local subhalo density

The LMC-analog perturbs the number density n_{sub} of subhalos in two distinct ways. Firstly, it introduces an anisotropically distributed subhalo population that is dragged along by the satellite’s motion. Secondly, it induces a response in the host DM halo.

As the LMC approaches its first pericentric passage, the inner galaxy (consisting of the disk and halo system within 30 kpc) reacts more rapidly than the outer galaxy, resulting in a relative displacement between the two reference frames: the inner and outer galaxy frames. This displacement gives rise to a north-south asymmetry in density, which is referred to as the collective response (Garavito-Camargo et al. 2021; Salomon et al. 2023). The collective response includes a large-amplitude weakly damped dipole mode, as well as several other low-amplitude modes (Weinberg 2022). Additionally, the satellite induces a trailing dynamical friction wake in the DM halo (Garavito-Camargo et al. 2019).

Fig. 9 illustrates the variation in the number of subhalos over time in each quadrant for the inner halo (0–50 kpc, top row) and the outer halo (50–100 kpc, bottom row) in the case of m12b with and w/o contributed subhalos (left and middle column, respectively), as well as for m12i (right column). The color bar at the bottom represents the quadrant location of the LMC during a time interval of ± 0.5 Gyr.

For m12i, the number of subhalos remains relatively consistent across all quadrants over time, except for Quadrant IV in the outer halo. In this quadrant, there is a systematically increased subhalo population, which can be attributed to the presence of an orbiting dwarf galaxy.

In the case of m12b, we identify the specific effects that contribute to perturbations in the number of subhalos within a time interval of approximately ± 0.5 Gyr.

- **contributed subhalos:** We observe a relative increase in the number of subhalos in the outer halo Q. IV (between -0.25 to 0 Gyr), Q. I (between 0 to 0.2 Gyr), and Q. II (0.2 Gyr onwards) when comparing the left and middle columns. Additionally, there are enhancements in Q. I of the inner halo at 0 Gyr, corresponding to the satellite being at a pericenter distance of 38 kpc.
- **Collective response:** A significant overdensity is observed in the outer halo (middle column), primarily in Q. II, as the satellite approaches pericenter from Q. IV (starting from approximately -0.5 Gyr).

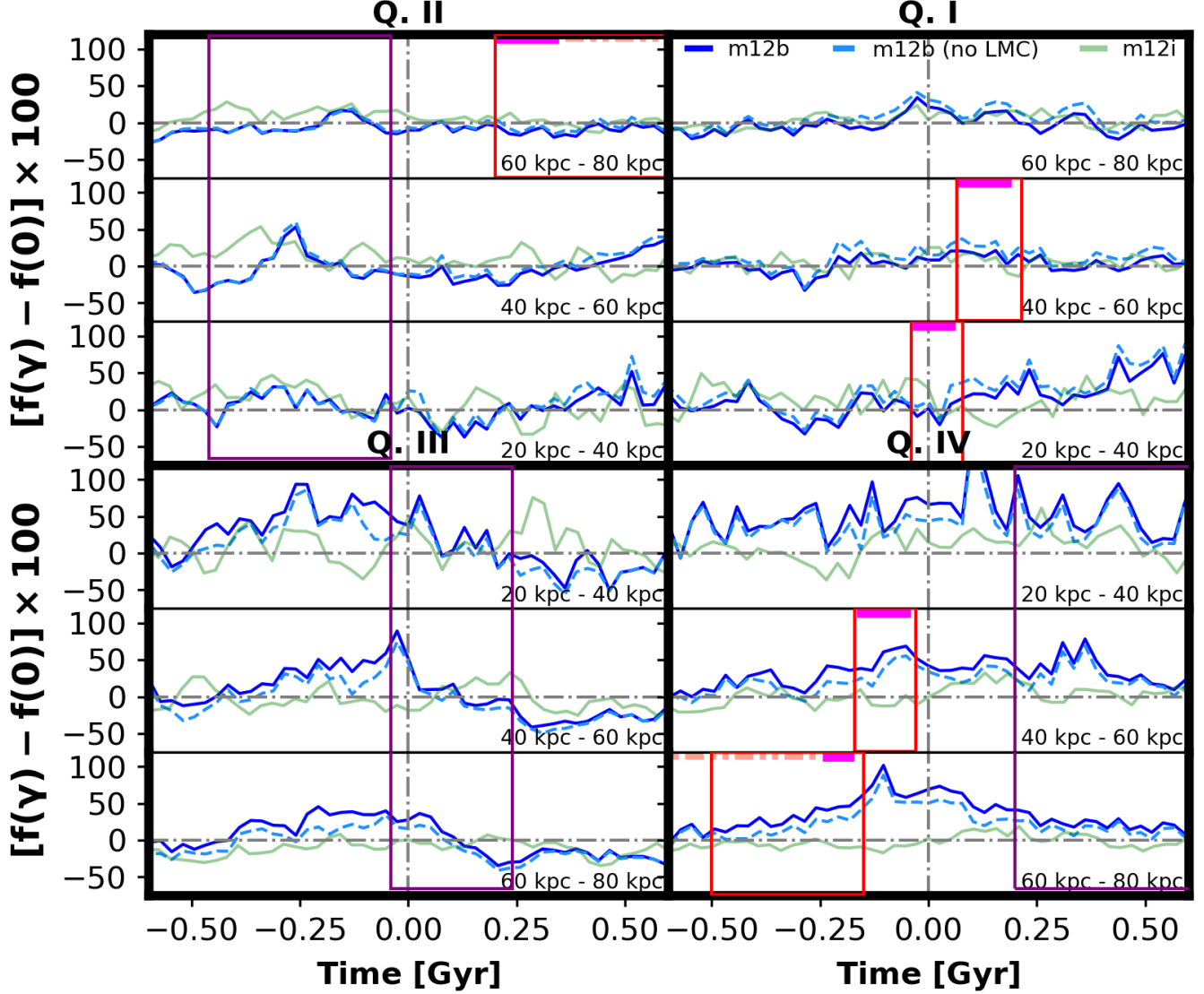


Figure 8. $[f(\gamma) - f(0)] \times 100$ (refer to Eq.13) (in Galactocentric coordinates) is plotted as a function of time for m12b with contributed subhalos (dark blue), m12b w/o contributed subhalos (light blue), and m12i (green) evaluated in different quadrants from Table. 2, within distance limits between 20-80 kpc at intervals of 20 kpc, and in Galactocentric coordinates arranged as a Cartesian plane. The position of the LMC-analog is tracked in each panel, indicated by a solid magenta bar, with a dashed cherry tomato bar used when the analog is outside the distance bins. The regions with an influx of contributed subhalos are marked with a red box in the corresponding panels, while the regions where reflex motion is expected are marked with a purple box. These values in Galactocentric coordinates are attributed to a stream in a fully circular orbit at the center of each distance bin in the respective quadrant.

- **DM dynamical friction wake:** The middle column shows a consistent number of subhalos after the LMC-analog leaves a specific quadrant. In the outer halo, the subhalos predominantly trail the LMC-analog in Q. IV (near 0 Gyr) and Q. I (between 0.25 to 0.35 Gyr).

These effects collectively contribute to the observed perturbations in the number density of subhalos and their respective quadrants within the specified time interval for m12b.

4. ENCOUNTER RATES FOR SIMULATED AND REAL STREAMS

In this section, we present our results for stream–subhalo encounter rates for the synthetic streams (Sec. 4.1) and the MW streams (Sec. 4.2). These encounter rates are calculated using Eq.13 for each time step along the integrated stream orbits. We subsequently compute the encounter rates per Gyr using Eq.14. In all cases we utilize both the traditional approach involving setting $\bar{\mu} = 0$, denoted as encounter rates w/o $\bar{\mu}$, and the calculation of $\bar{\mu}$ using subhalo kinematics as

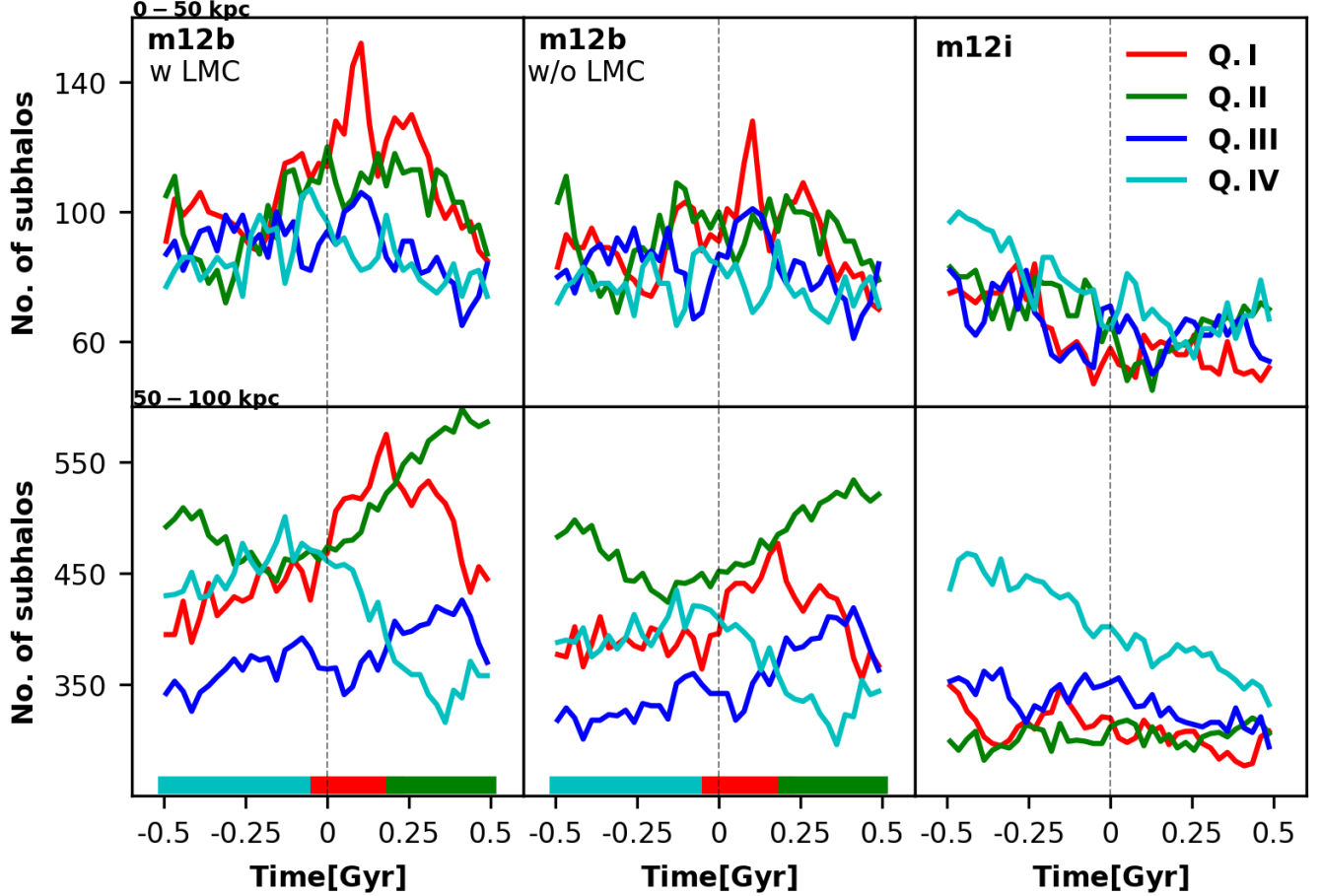


Figure 9. Number of subhalos in each quadrant (defined in Table 2) as a function of time within a time interval of ± 0.5 Gyr around the first pericenter of the LMC. The top row shows the subhalos in the inner halo (0–50 kpc), while the bottom row shows the subhalos in the outer halo (50–100 kpc). In m12b, we see large variations in the number of subhalos as a function of time. For example, prior to pericenter (-0.5 Gyr onwards), when the LMC-analog is moving from Q. IV to Q. I, the number of subhalos sharply peaks in Q. II (opposite quadrant) in the middle panel. Looking at the left panel, in Q. I the number of subhalos increases after pericenter where the LMC-analog moves to, while in Q. IV the number of subhalos decreases after pericenter when then LMC-analog leaves Q. IV. These changes are the results of the combination of the DM halo response (DM wake and collective response).

described in Eq. 13. For the m12b system, we further compute encounter rates by excluding contributed subhalos, denoted as encounter rates w/o LMC. Our simulations are limited by the subhalo resolution and the presence of artificial disruption near the LMC-analog (van den Bosch et al. 2018; Green et al. 2021), which might lead to a systematic underestimation of subhalo number densities, and therefore the encounter rates. Barry et al. (2023) showed that increasing the particle resolution by a factor of 8 did not affect the number density of subhalos significantly.

4.1. Encounter rates of synthetic streams

We analyze the encounter rates for 5000 synthetic streams introduced in Sec. 2.5. Here we present statistically averaged encounter rates as a function of three main stream properties. 1) galactocentric distance; 2) Stream location on the sky, as defined by the quadrant; 3) The stream’s angular momen-

tum direction relative to the LMC-analog’s in m12b angular momentum.

4.1.1. Dependence on pericenter distance and sky location

The encounter rates depend linearly on the multiplication of number density of subhalos n_{sub} and the velocity dispersion of subhalos in stream-centric coordinates, both of which decrease as a function of galactocentric distance. Barry et al. (2023) noted that number density of subhalos is constant as a function of distance from the center out to 60 kpc at present day but we see a decreasing trend in number density around our integration time which is roughly 5 Gyr before present day. However, the dominant factor is the multiple of number density and velocity dispersion which is decreasing at all times. Here we focus on the encounter rates dependency on the stream’s pericenter distance. In our orbit integration scheme, all the synthetic streams have a fixed pericentric dis-

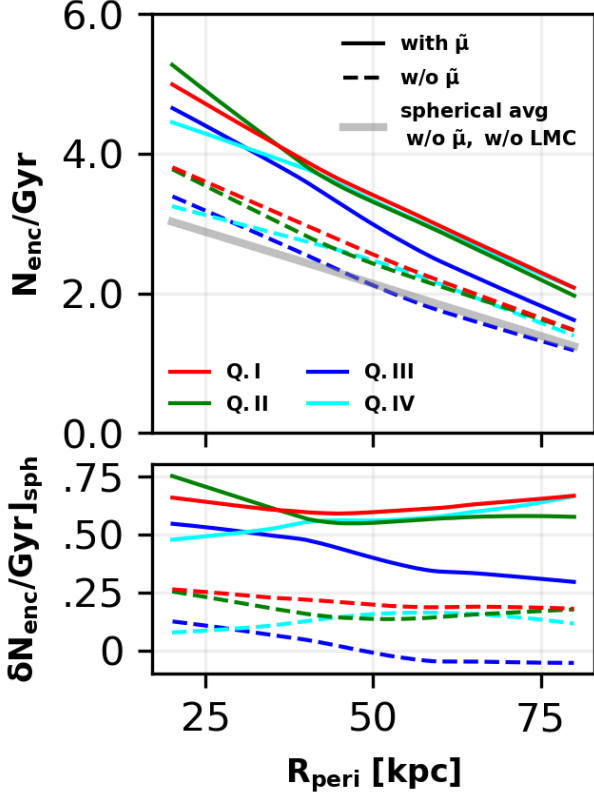


Figure 10. Estimated number of encounters per Gyr for a synthetic stream of length $\ell_s = 10$ kpc and impact parameter $b_{\max} = 1$ in m12b with $\tilde{\mu}$ (solid) and w/o $\tilde{\mu}$ (dashed). The encounters are plotted as a function of the stream’s pericenter distance at $T = 0$ Gyr and four quadrants (marked by colors). The gray line represents the range of encounter rates for m12b w/o $\tilde{\mu}$ and w/o contributed subhalos, as well as for m12i (re-scaled to match the m12b halo mass), averaged over all quadrants. These curves are estimated using a lowess regression (Cleveland & Devlin 1988) from the 5000 simulated stream data. Streams in Q. I and II have the highest potential for encounters, as the LMC’s position in m12b at $T = 0$ Gyr leads to a higher concentration of subhalos in Q. IV (at large distances) and Q. I, and the majority of reflex motion and collective response effects are dominant in Q. II. Q.III as expected has the lowest encounter rates of all. Second row plots the fractional changes in each encounter rates with respect to the spherically averaged rates w/o $\tilde{\mu}$ and w/o LMC.

tance at $T = 0$ Gyr. We computed the encounter rates in the quadrants defined in Figure 1 and in spherical shells (grey line). In all cases, the encounter rates are computed using lowess regression (Cleveland & Devlin 1988). The encounter rates for the m12b halo are shown in Fig. 10. Note that here we remove the contributed subhalos.

As expected, we find a decreasing trend in the number of encounters per Gyr ($N_{\text{enc}}/\text{Gyr}$) as the pericenter distance increases in all quadrants (represented by different colors). However, we find that the assumption of $\tilde{\mu} = 0$ (dashed

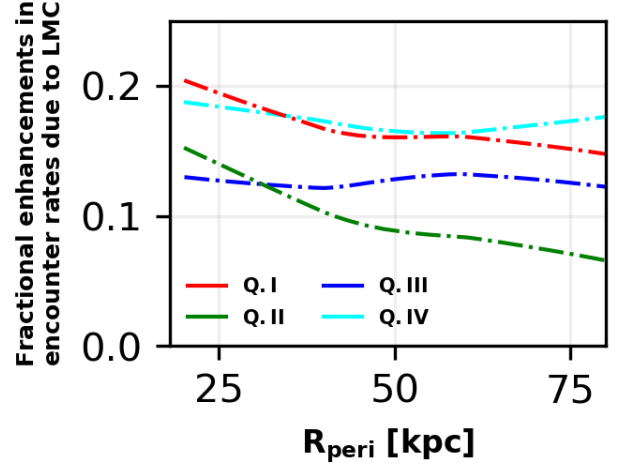


Figure 11. Fractional enhancements of encounter rates due to contributed subhalos from the LMC-analog as a function of distance in each quadrant for m12b in the integration time frame. In Q.I and Q.IV, the streams exhibit a consistent increase of approximately 20% in encounter rates across all distance ranges. This increment is attributed to the higher number density of contributed subhalos and changes in the radial velocity distribution parameters. In contrast, Q.II demonstrates a smaller difference of around 10% in encounter rates, as reflex motion in the outer halo dominates the encounter dynamics. Notably, Q.III displays a distinct peak at larger distances, indicative of the presence of trailing contributed subhalos. These subhalos can boost the encounter rates through the halo by 5-20%.

lines) and the location on the sky and have an impact on the encounter rates. Overall, the $N_{\text{enc}}/\text{Gyr}$ values with $\tilde{\mu}$ consistently exhibit enhancements between 25%-75% higher compared to rates w/o $\tilde{\mu}$.

We find variations in the encounter rates between different quadrants for both cases with $\tilde{\mu} = 0$ and computing $\tilde{\mu}$ from the simulations. Q. I and II show the highest increment in encounter rates compared to the spherically averaged rates with $\tilde{\mu} = 0$ (gray line), with increases of up to 60–70% (bottom panel). The increased encounter rates in Q. I can be attributed to the higher number density of subhalos and the changes in effective $\tilde{\gamma}$ (given by $\tilde{\mu}/\sqrt{2\tilde{\sigma}}$) caused by the leading contributed subhalos from the LMC-analog. Q. II exhibits higher encounter rates due to the collective response and reflex motion. Q. IV shows a relative increase at larger distances due to the presence of contributed subhalos and the influence of the DM wake. Q. III has the lowest encounter rates as none of the boosting effects are prominent in Q. III. On the other hand, m12i (not shown here) has no quadrant dependence and the encounter rates with $\tilde{\mu}$ are higher by 20% when compared with $\tilde{\mu} = 0$. We note even without an LMC-analog, $\tilde{\mu} = 0$ is generally non-zero, similarly Cunningham et al. (2019) showed that velocity isotropy changes as a function of position on the sky.

4.1.2. LMC-analog contribution to the encounter rates

In Fig. 11, we present the fractional enhancements in $N_{\text{enc}}/\text{Gyr}$ resulting from the presence of contributed subhalos in m12b. These enhancements are computed by assessing the differences between encounter rates with $\tilde{\mu}$ in the presence of contributed subhalos and encounter rates without these subhalos, using lowess regression. Notably, the trends in fractional enhancements for encounter rates without $\tilde{\mu}$ follow similar patterns to those with $\tilde{\mu}$.

The plot reveals the extent of these enhancements across different distances in each quadrant, depicted by distinct line colors. It is evident that contributed subhalos have a more pronounced impact on encounter rates in Q.I and Q.IV, yielding a substantial increase of nearly 20–40% (appendix. .1). This observation aligns with the findings from the first row of Fig. 5, which emphasize the significant influence of contributed subhalos in these quadrants. In contrast, Q.II within the inner halo and Q.III in the outer halo exhibit relatively lower enhancements, with values not exceeding 11%. Notably, Q.II in the outer halo showcases the least enhancement, as encounter rates at larger distances are primarily influenced by bulk motion effects. We note higher localized boost of about 40% for another LMC-analog system in appendix. .1 where the LMC-analog falls in closer to the present day (Barry et al. 2023).

In summary, our analysis highlights the crucial role of subhalo–stream kinematics, particularly the relative radial motion of subhalos in relation to a stream ($\tilde{\mu}$), as a key factor in accurately predicting encounter rates. This results in a minimum overall enhancement of 25%. Moreover, we observe a notable dependence of encounter rates to the location in the sky. Q. I and IV experience additional enhancements of nearly 20–40%, driven by the presence of contributed subhalos, while Q. II shows increased rate due to the interplay of collective response and reflex motion effects. These findings illuminate the critical significance of subhalo–stream kinematics and provide profound insights into the underlying dynamics governing stream–subhalo interactions within the MW–LMC system.

4.1.3. Dependence on streams’ orientation and orbit.

As shown in previous sections, the presence of a massive satellite disrupts spherical symmetry, which, in itself, is not a particularly great approximation. Consequently, this disruption introduces a dependence of stream–subhalo encounter rates on the specific sky location of the streams. In this section, we further explore the sensitivity of encounter rates to the streams’ orbit’s sense of rotation and eccentricity. We categorize the sense of rotation of synthetic stream orbits relative to the LMC-analog orbit. Additionally, the eccentricity is computed within the Galactocentric frame. Among the 5000 synthetic streams, approximately 50% exhibit retrograde orbits relative to the LMC-analog’s orbit, while the remaining 50% are in prograde orbits.

Our analysis reveals no measurable correlation or dependence of interaction rates on eccentricity for either orbit type in any quadrant. However, we observe that the stream–subhalo interactions implicitly depend on the streams sense of

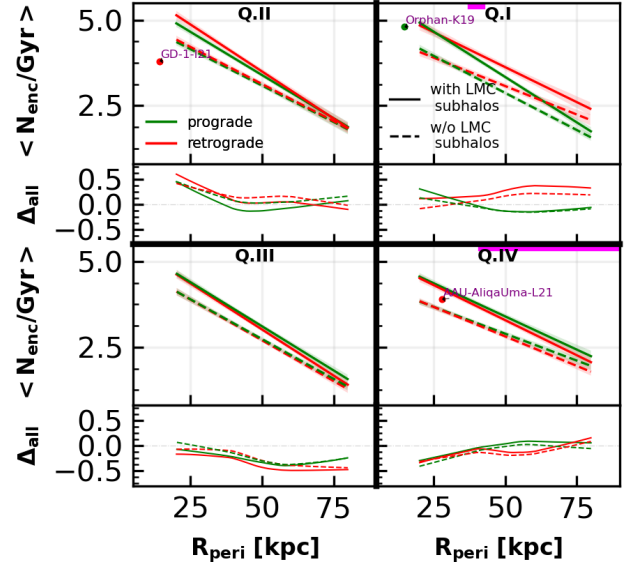


Figure 12. The average encounter rate (row 1 and 3) is estimated using separate robust regressions (Wilks 1938; Huber 1973) for prograde (green) and retrograde (red) streams, taking into account the stream’s pericenter distance and sky position (quadrants marked on subplots). These calculations are performed in m12b with (solid) and without (dashed) contributed subhalos from the satellite. The difference with respect to the spherical average, denoted as Δ_{all} , is also shown in rows 2 and 4. The magenta bar represents the LMC distance in each quadrant within the time frame when encounter rate calculation was done. Additionally, the encounter rates for the MW streams GD-1, Orphan, and AliqUma, categorized by their orbit types, are shown in their respective quadrants. It is important to note that the streams are plotted as a function of their present-day distance in the m12b Galactocentric frame. We note that streams in retrograde orbits with respect to the LMC-analog consistently exhibit higher encounter rates in northern hemisphere (regions polar opposite to the analog trajectory.)

rotation. This is shown in Figure 12, where the encounter rates averaged over all streams in a distance bin for each quadrant independently ($\langle N_{\text{enc}}/\text{Gyr} \rangle$) as a function of distance in each quadrant for prograde (green) and retrograde (red) stream orbits. These rates are computed using robust regression (Wilks 1938; Huber 1973) in m12b with and w/o contributed subhalos, represented by solid and dashed lines, respectively. The sub-panels below each quadrant display the Δ_{all} , which represents the difference between the average encounter rates in each quadrant for each orbit type (i.e prograde and retrograde with respect to the LMC-analog) and the spherically averaged encounter rate for both orbit types, with and w/o contributed subhalos. The magenta bar in specific panels indicates the distance limits of the LMC within each quadrant during the calculation of encounter rates.

Retrograde orbits with respect to the LMC-analog consistently exhibit higher encounter rates (approximately 0.25 -

0.75 more encounters) in the northern hemisphere (mostly in Q.I) compared to prograde orbits, regardless of the presence of contributed subhalos. This higher encounter rate can be attributed to the relative bulk motion of subhalos, which aligns in the same direction as retrograde stream orbits in Q.I and Q.II, thereby increasing the likelihood of encounters.

The Δ_{all} panel reveals that retrograde streams in Q.I (ahead of LMC pericenter distance) and Q.II (behind LMC pericenter distance) have encounter rates nearly 0.5 encounters higher than the spherically averaged across orbit kind and about 50% higher than spherically averaged gray shaded line shown in Fig. 10. Prograde streams exhibit overall lower enhancement in encounter rates.

In contrast, the dependence of encounter rates on orbit type in Q.IV is more complex, as the LMC spends the majority of the integration time in this quadrant. Prograde orbits in the outer regions of Q.IV experience a higher average number of encounters (approximately 0.15 more encounters) due to their motion aligning with that of the LMC. This alignment increases the likelihood of encountering subhalos, as the streams spend more time in close proximity to the contributed subhalos. Additionally, the presence of a transient DM wake can further contribute to the increased encounter rates for prograde orbits in the outer regions of Q.IV.

In the absence of contributed subhalos, encounter rates exhibit similar trends for both orbit types except in Q.I, and the relative difference between the two orbits is lower, as shown by the dashed curves in Δ_{all} . It is important to note that encounter rates with $\mu = 0$ do not exhibit any trends between different orbit types in any of the quadrants, not even in Q.I. However, introducing a non-zero μ , complicates the systematic view. This is because the direction of the stream's apparent motion affects $f(\tilde{\gamma})$ (from Eq. 14), which can both increase and decrease the encounter rates, as shown in Fig. 4.

We annotate the GD-1 stream (Grillmair & Dionatos 2006), the Orphan stream (Grillmair 2006; Belokurov et al. 2007; Koposov et al. 2019), and the AliqaUma stream (Li et al. 2021b) in their respective quadrants and orbit types relative to the LMC analog. The trends observed in our synthetic streams generally align with those observed in the MW streams. In particular, the Orphan-Chenab stream closely interacts with the LMC and extends across both hemispheres of the MW (Koposov et al. 2023). Additionally, Lilleengen et al. (2023) has demonstrated the effects of the deforming MW halo on the proper motion and morphological structure of streams, making it challenging to differentiate between changes caused by subhalo-stream interactions and other influences.

4.2. Encounter rates of MW streams

We have observed that synthetic streams around halos with LMC-like satellites display a diverse range of encounter rates, contingent upon several factors: 1) The specific value of $\tilde{\mu}$ associated with the stream; 2) stream's location in the sky; and 3) The orbital rotation direction in relation to the LMC-analog's orbit. Notably, our findings demonstrated elevated encounter rates for orbits located in the northern hemisphere, and in regions near the LMC and diametrically opposed to it.

Expanding upon our analysis, we now proceed to calculate encounter rates for all MW streams within our simulation. We employ the same orbital integration methodology as employed for synthetic streams. However, for MW streams, we substitute the initial conditions with the present-day phase-space coordinates of each stream in the MW. To establish these initial conditions, we utilize the median position and velocity of each stream track. We further adjust these conditions by applying a rotation that emulates the orientation of actual streams relative to the real LMC as discussed in Sec. 2.5.

Our results are summarized in Table 3, we present the computed encounter rates ($N_{\text{enc}}/\text{Gyr}$) in both m12b and m12i for known MW streams (Mateu 2023). The table also includes the orbital properties of each stream, such as its present-day distance from the host galaxy (d) and the sky quadrant (Q) it occupies at $T = 0$ Gyr. However, it is important to note that these properties are calculated within the simulated m12b potential and may not directly correspond to the real MW. The eccentricity of the orbit (e) and its grade (G) with respect to the LMC analog in m12b are also provided. The grade indicates whether the stream's motion is prograde (in the same direction as the LMC orbit, denoted by "+") or retrograde (opposite to the LMC orbit, denoted by "-"). These properties are calculated using the m12b potential models of DM halo and baryonic disks from Arora et al. (2022). It is crucial to emphasize that around 75% of the MW streams are situated within a radius of 20 kpc at $T = 0$ Gyr. While interpreting these encounter rates, it's important to be cautious due to the limited resolution in the inner regions. Barry et al. (2023) showed that the total subhalo population within a 50 kpc radius, 5 Gyr ago, was approximately twice as high for subhalos with $M_{\text{sub}} \geq 10^6 M_{\odot}$ compared to the present-day population. As a result, we can adjust our encounter rates by dividing them by a factor of 2. For example, they estimated that the GD-1 stream, with a length of 15 kpc with an average impact parameter of 1.5 kpc, could experience approximately 5 encounters per Gyr using traditional symmetry and isotropy assumptions. With the inclusion of LMC-induced subhalos, this rate increases twofold. In our analysis, our re-scaled for present day encounter rates for the same stream length and impact parameter is 3.5 encounters per Gyr for m12i and 4.3 encounters per Gyr for m12b. These numbers are more or less similar because m12i has about 1.2 times less subhalos than m12b without the LMC-contributed subhalos. Given the location in the sky and distance from the center of GD-1, we don't expect any boosts in encounter rates due to the LMC and our numbers are consistent with Barry et al. (2023) to first order.

Among the MW streams analyzed, the Aquarius-W11 stream (Williams et al. 2011), Lethe-G09 (Grillmair 2009), and Phlegethon-I21 (Ibata et al. 2021) in the inner halo (within 30 kpc) exhibit the highest encounter rates within the m12b simulation. Conversely, the Cetus-Y13 stream (Yam et al. 2013) has the highest encounter rate in the outer halo (at distances greater than 30 kpc). The streams C-7-I21 (Ibata et al. 2021), Ophiuchus-C20 (Caldwell et al. 2020), and

OmegaCen-I21 (Ibata et al. 2021) have the lowest encounter rates among the analyzed streams. These streams are located in the inner halo, orbiting within 7 kpc of the galactic center. Additionally, the Eridanus-M17 stream (Myeong et al. 2017), positioned at a distance of 100 kpc, exhibits the lowest encounter rates compared to other streams.

Overall, we observe consistent encounter rate trends for MW streams across m12i and m12b, both with and without $\tilde{\mu}$. Streams situated beyond a present day distance of 20 kpc in the m12b exhibit a clear dependence on location, with enhanced encounter rates in Q, II and IV. Conversely, the m12i demonstrates no azimuthal dependence in encounter rates. Furthermore, incorporating $\tilde{\mu}$ yields approximately a 30% boost in encounter rates for both m12b and m12i. The sense of rotation of the streams does not notably impact the encounter rates, mainly due to the proximity of these streams to the galactic center while these effects are prominent for streams positioned in the outer halo regions.

Table 3. Encounter rates of the MW streams in m12b and m12i

Name	d* [kpc]	Q*	G	e	Enc. rates	
					m12b	m12i
20.0-1-M18	20.0	IV	-	0.3	4.3	4.0
300S-F18	20.6	II	+	0.6	4.4	2.6
AAU-ATLAS-L21	23.1	IV	-	0.5	3.7	4.3
AAU-AliqaUma-L21	27.9	IV	-	0.5	3.9	4.2
ACS-R21	18.7	II	+	0.1	4.6	2.8
Acheron-G09	6.1	II	+	0.2	3.0	3.0
Alpheus-G13	8.0	II	-	0.1	2.5	2.6
Aquarius-W11	8.1	III	+	0.6	7.5	3.7
C-19-I21	20.8	III	+	0.5	3.1	3.0
C-4-I21	10.1	III	-	1.0	4.1	2.6
C-5-I21	12.1	II	+	0.8	3.9	2.1
C-7-I21	4.0	III	+	0.4	1.0	2.5
C-8-I21	7.0	II	-	0.4	4.9	3.5
C-9-I21	12.1	III	-	0.1	3.9	3.1
Cetus-New-Y21	20.8	IV	-	0.3	4.5	3.0
Cetus-Palca-T21	34.6	IV	-	0.4	3.2	2.7
Cetus-Y13	35.3	III	-	0.2	4.5	3.6
Cocytos-G09	9.6	II	+	0.2	3.5	3.5
Corvus-M18	11.0	II	+	0.5	5.1	2.7
Elqui-S19	50.1	IV	-	0.5	3.4	3.7
Eridanus-M17	100.0	I	-	0.6	0.7	0.7
GD-1-I21	14.2	II	-	0.1	3.8	3.1
Gaia-1-I21	8.2	II	-	0.6	6.4	2.9
Gaia-10-I21	18.4	II	-	0.1	4.9	3.1
Gaia-11-I21	12.0	III	-	0.9	3.5	3.5

Continued on next page

Name	d* [kpc]	Q*	G	e	Enc. rates	
					m12b	m12i
Gaia-12-I21	18.2	III	+	0.3	2.6	3.1
Gaia-2-I21	10.8	III	-	0.2	3.8	3.5
Gaia-3-M18	12.9	II	+	0.6	6.1	2.7
Gaia-4-M18	14.5	II	+	0.5	5.5	2.5
Gaia-5-M18	25.5	II	+	0.2	4.7	2.6
Gaia-6-I21	10.4	II	-	0.2	5.0	2.2
Gaia-7-I21	8.7	II	+	0.4	3.6	2.3
Gaia-8-I21	8.6	II	-	0.3	4.0	2.1
Gaia-9-I21	9.4	II	+	0.9	3.7	3.9
Gunnthra-I21	6.3	II	+	0.4	2.3	2.7
Hermus-G14	17.3	II	+	0.5	5.6	3.3
Hrid-I21	8.0	III	-	0.9	5.9	3.8
Hyllus-G14	17.4	III	+	0.5	5.9	3.7
Indus-S19	13.6	IV	+	0.2	4.2	4.0
Jet-F22	34.0	II	-	0.7	3.9	2.7
Jhelum-a-B19	11.3	IV	+	0.6	3.9	5.0
Jhelum-b-B19	11.4	IV	+	0.6	3.9	5.1
Kshir-I21	14.8	III	-	0.6	3.9	3.2
Kwando-G17	22.9	IV	-	0.2	3.9	3.0
LMS1-Y20	12.4	II	+	0.6	3.9	2.2
Leiptr-I21	13.7	II	+	0.7	4.4	3.1
Lethe-G09	13.3	II	+	0.2	5.1	3.0
M2-I21	9.8	III	+	0.9	3.4	2.8
M30-S20	7.0	III	-	0.3	4.4	3.2
M5-G19 [†]	13.7	II	-	-	6.6	3.9
M68-P19	8.9	II	+	0.4	3.5	3.5
M92-I21	10.3	III	-	0.6	3.1	3.0
Molonglo-G17	21.0	IV	-	0.2	4.1	3.1
Monoceros-R21	18.2	II	+	0.1	4.5	2.6
Murrumbidgee-G17	21.0	IV	-	0.3	3.7	3.2
NGC1261-I21	21.4	I	+	0.9	4.6	3.9
NGC1851-I21	17.8	I	+	0.7	3.4	2.8
NGC2298-I21	17.4	II	+	0.9	4.4	4.1
NGC288-I21	13.7	IV	+	0.6	5.8	1.8
NGC3201-P21	11.0	II	+	0.6	4.9	3.2
NGC5466-G06	17.5	II	+	0.2	5.2	2.4
NGC6362-S20	5.0	I	-	0.7	6.2	2.1
NGC6397-I21	5.9	II	-	0.5	2.0	1.2
OmegaCen-I21	7.0	II	-	0.4	1.0	1.2
Ophiuchus-C20	4.3	II	-	0.8	1.8	0.5
Orinoco-G17	22.2	IV	-	0.2	3.6	3.2
Orphan-K19	14.8	I	+	0.2	4.8	3.3

Continued on next page

Name	d* [kpc]	Q*	G	e	Enc. rates	
					m12b	m12i
Pal13-S20	24.8	III	-	0.6	4.5	3.2
Pal15-M17	31.6	IV	+	0.3	4.0	2.1
Pal5-PW19	16.6	II	-	NaN	6.9	6.0
Palca-S18	37.5	IV	-	0.2	2.8	3.0
Parallel-W18	16.9	II	+	0.4	5.2	2.5
Pegasus-P19	18.6	III	-	0.7	5.5	2.8
Perpendicular-W18	17.5	II	+	0.2	5.5	2.3
Phlegethon-I21	6.7	III	+	0.6	7.0	3.7
Phoenix-S19	18.5	IV	-	0.2	3.6	3.6
PS1-A-B16	13.6	III	-	0.1	3.8	2.9
PS1-B-B16	18.7	II	+	0.5	5.4	2.7
PS1-C-B16	17.5	III	-	0.7	5.5	3.6
PS1-D-B16	28.1	II	+	0.5	4.0	3.1
PS1-E-B16	17.6	II	+	0.2	5.5	2.3
Ravi-S18	19.7	IV	-	0.8	4.1	3.8
Sagittarius-A20	8.3	IV	-	0.9	3.1	4.3
Sangarius-G17	27.1	II	+	0.4	4.5	3.3
Scamander-G17	26.1	II	+	0.4	4.2	2.8
Slidr-I21	9.4	II	-	0.5	3.7	3.0
Styx-G09	42.3	II	+	0.3	2.7	1.4
Svol-I21	7.8	II	+	0.3	3.4	3.7
Sylgr-I21	8.7	II	-	0.3	4.8	2.2
Tri-Pis-B12	31.4	III	-	0.4	4.3	2.9
TucanaIII-S19	23.1	IV	-	0.7	3.6	4.8
Turbio-S18	17.6	IV	-	0.5	4.5	3.1
Turraburra-S19	32.9	I	-	0.7	2.7	3.3
Vid-I21	26.3	IV	-	0.3	3.0	3.7
Wambelong-S18	19.5	I	+	0.6	4.0	2.8
Willka_Yaku-S18	34.4	I	-	0.4	2.2	2.3
Ylgr-I21	11.9	II	-	0.8	4.9	2.3

d: distance of the stream from the MW. Q: Quadrant in the sky, rotated to match relative positions with LMC analog in m12b. G: Orbit's motion, prograde (+) or retrograde (-) with respect to the LMC orbit in m12b. e: eccentricity of the stream orbit in m12b. Streams with encounter rate ratios of at least 2 between m12b and m12i are highlighted in bold.

*Computed at $T = 0$ Gyr.

† Missing proper motion information in `galstreams`.

Note that Barry et al. (2023) demonstrated that the total subhalo population within a 50 kpc radius 5 Gyr ago was nearly twice as higher than the present-day population. Therefore our rates can be extrapolated to present day by appropriately scaling them down by a factor of 2.

5. DISCUSSION: THE MILKY WAY IN CONTEXT

Currently there are ≈ 100 observed streams in the MW. However, in the next decade we expect to discover more streams, specially in the outer halo thanks for upcoming surveys such as LSST (Ivezić et al. 2019). Furthermore we will have a multidimensional view of the phase-space and kinematics of the streams to unprecedented accuracy. As such,

the search for disturbances from DM subhalos can be done systematically across large areas on the sky. With the insight from previous sections, we can now predict which areas on the sky in the MW where we might find streams with higher probabilities of having been perturbed by subhalos.

We made use of the orbital integration of the synthetic streams in the m12b halo potential to compute encounter rates across the halo. The system is rotated in such a way that the massive satellite is roughly in the same location as the real LMC at present day and also the orbits are approximately identical. We then identify the regions in the sky where streams between 20-80 kpc, would experience higher probabilities of interacting with subhalos. In Fig. 13, we highlight the specific regions in the sky with increased probability of detecting stream-subhalo interactions.

These regions are identified by analyzing the sky positions of synthetic streams at $T = 0$ Gyr in m12b, considering the expected changes with and w/o the presence of contributed subhalos. These regions are shaded manually by running a k-means clustering algorithm on stream location (MacQueen 1967), dividing the stream positions in galactocentric coordinates into three distinct groups: one group for the background, another for reflex motion, and a third for leading LMC subhalos categories, while also removing any outliers.

The red-shaded region represents the polar opposite region to the LMC, where the dominant effect on stream-subhalo interactions is the reflex motion response, both in position and velocity. The purple-shaded region indicates a higher subhalo density due to the presence of LMC dark matter subhalos in the leading debris and the LMC itself. Streams located within these shaded regions are expected to have a higher likelihood of encounters with subhalos. Our estimates based on Sec. 4 suggest an enhancement ranging from 25% to 75% (depending on the stream's orbital orientation (Fig. 12)) in the reflex motion region (red shaded area) and from 15% to 60% in the region influenced by the leading LMC subhalos (see Fig. 10, 11) (purple shaded area).

Additionally, we include MW streams orbiting beyond 20 kpc from the galactic center, with encounter rates greater than the 90th percentile limit (4.4 encounters per Gyr) based on our calculations in m12b (see Table 3). We predict that streams such as NGC1261-I21 (Ibata et al. 2021), Scamander-G17 (Grillmair 2017), Sangarius-G17 (Grillmair 2017), AAU-AliqaUma-L21 (Li et al. 2021b), Cetus-Y13 (Yam et al. 2013), and Gaia-5-M18 (Malhan & Ibata 2018) have the highest likelihood of interactions in the outer regions of the stellar halo. Furthermore, it is worth noting that the Aliquama/Atlas stream along with other globular cluster streams that are within the shaded regions are promising targets for the Large Synoptic Survey Telescope (LSST) (Ivezić et al. 2019) and other future surveys.

These predictions can be valuable for observing strategies aimed at detecting spurs, kinks, and gaps in streams during future surveys, particularly in the outer regions of the halo. Surveys such as the Vera Rubin Observatory (Ivezić et al. 2019), Nancy Grace Roman Space Telescope (Spergel et al. 2013, 2015), DESI (Collaboration et al. 2016a), WEAVE

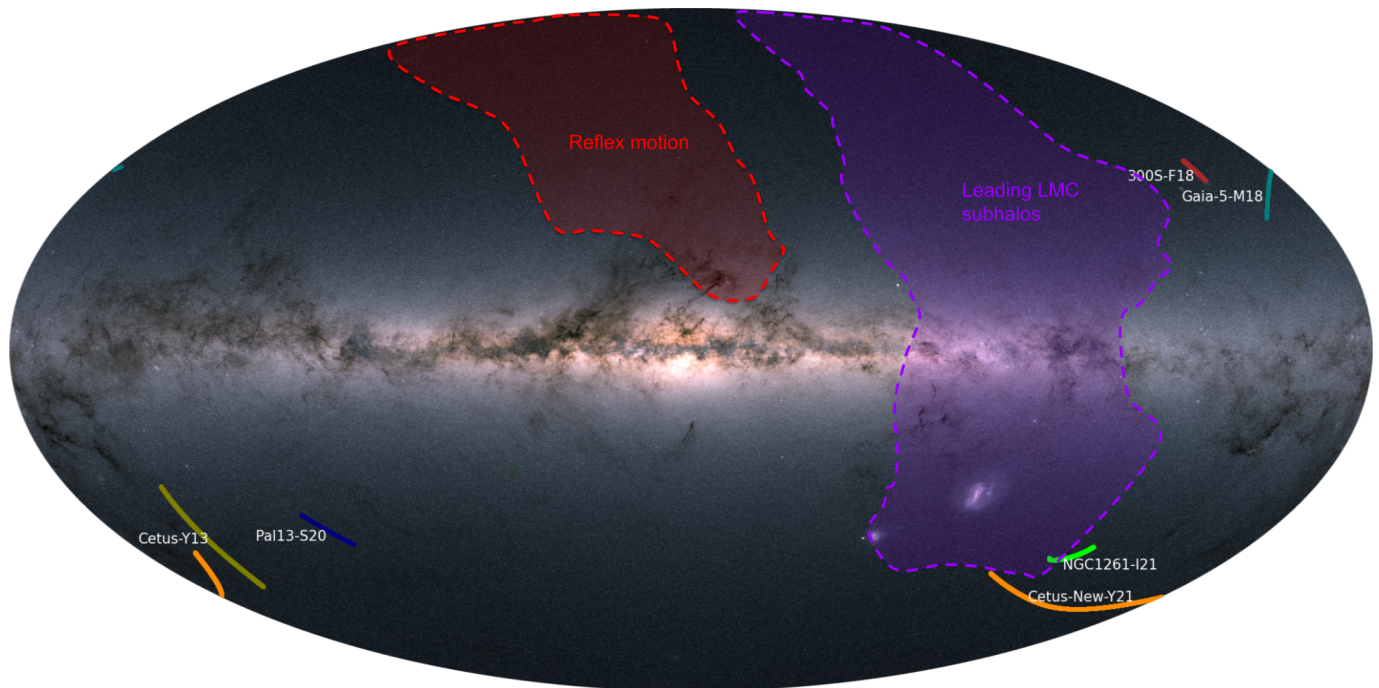


Figure 13. Regions where we expect the LMC to enhance the encounter rate of streams with subhalos, superimposed on the stellar flux map from Gaia DR2 (Gaia et al. 2018). Shaded regions on the map indicate higher overall probabilities of encounter rates, which have been determined using the top 1% synthetic streams in m12b, rotated to align with the MW-LMC orientation at present day. To aid visualization, the synthetic streams have been color-coded using a k-means clustering algorithm (MacQueen 1967), and shaded regions have been manually drawn. Milky Way (MW) streams located at distances greater than 20 kpc, which are expected to have the highest encounters based on their positions relative to the LMC-analog (as noted in m12b), are plotted on the map. Streams within the shaded regions labeled as reflex motion (red) and subhalos brought in by the LMC (purple) are anticipated to have a higher probability of subhalo-stream interactions.

(Dalton et al. 2012), 4MOST (De Jong et al. 2019), Subaru PFS (Takada et al. 2014), among others, can prioritize regions in the sky where streams are more likely to have encounters with subhalos. It’s important to note that caution is required when interpreting these values as calibration benchmarks for specific stream regions. Instead, they offer insight into the potential systematic uncertainties that can arise from departures from equilibrium assumptions in these measurements.

6. CONCLUSIONS

In this paper, we have investigated the impact of a massive satellite on the encounter rates between stellar streams and dark matter subhalos. Leveraging two representative systems from the FIRE-2 hydrodynamical zoom-in simulations—one featuring an LMC-analog and the other lacking massive satellites—we address two key questions. First, we evaluated how the LMC-analog’s subhalo population contributes to enhancing encounter rates with host stellar streams building on the work of Barry et al. (2023) using the same simulations. Second, we investigated how the host halo’s response influences encounter rates galaxy-wide.

Our findings indicate a general decrease in encounter rates with increasing pericentric distance, independent of the eccentricity of stream’s orbit. The presence of a massive satellite, such as the LMC-analog, introduces asymmetry, resulting in varying encounter rates for streams across different

regions of the sky relative to the satellite. Key factors influencing these asymmetric effects are ranked as follows:

1. **Relative Radial Motion ($\tilde{\mu}$):** The relative radial motion of subhalos with respect to streams, represented by $\tilde{\mu}$, consistently enhances encounter rates by at least 30% even in systems without LMC-analog. Under the influence of an LMC-analog, localized boosts can jump up to 70% as observed in Q.II, compared to the spherically symmetric and $\tilde{\mu} = 0$ rates (Fig. 10).
2. **Contribution from LMC-analog subhalos:** The LMC-analog brings its own set of subhalos with unique phase-space orbits, as depicted in Fig. 5. These subhalos can boost the encounter rate up to 20–40% in Q.IV and Q.I, aligned with the LMC-analog’s motion (Fig. 11). This boost may be much higher in the MW today (appendix .1). Barry et al. (2023) showed that the number density can be boosted up to a factor of 2 due to the LMC–mass satellites.
3. **Orbital Alignment:** Streams in retrograde orbits with respect to the LMC-analog and located in the outer halo and opposite hemisphere exhibit enhanced rates up to 30%, with the most substantial boosts occurring in Q.I compared to prograde streams (Fig. 12).

In conclusion, our investigations reveal that streams situated in proximity to the LMC and in regions opposite to it are more likely to interact with subhalos, potentially leading to morphological changes. Building upon this insight, we have identified regions within the MW–LMC celestial sphere likely to display signatures of stream–subhalo interactions, as depicted in Fig. 13. Detecting such signatures and constraining the perturbing subhalo masses will offer valuable insights into allowed DM models with specific subhalo mass scales. Furthermore, our results emphasize the complexities introduced by the presence of a massive satellite such as the LMC, suggesting that the MW might not be an ideal laboratory for constraining the subhalo mass function due to the need to consider departures from the equilibrium assumptions. In this context, finding globular cluster streams orbiting in galaxies in a state of dynamical equilibrium present promising opportunities for precise constraints on the DM subhalo mass function. With upcoming missions like the Roman Space Telescope (Spergel et al. 2013, 2015), we anticipate the detection of such streams in other galaxies (Pearson et al. 2022; Aganze et al. 2023), enhancing our ability to derive valuable insights into the nature of dark matter.

Software: Astropy (Astropy Collaboration et al. 2013, 2018, 2022), IPython (Perez & Granger 2007), Matplotlib (Hunter 2007), Numpy (Harris et al. 2020), Pandas (Wes McKinney 2010), Scipy (Virtanen et al. 2020), Healpy (Zonca et al. 2019), consistent-trees (Behroozi et al. 2012b), rockstar (Behroozi et al. 2012a), halo_analysis (Wetzel & Garrison-Kimmel 2020a), gizmo_analysis (Wetzel & Garrison-Kimmel 2020b), Galstreams (Mateu 2023), AGAMA (Vasiliev 2019).

1 The authors thank Denis Erkal, Gurtina Besla, Kathryn V.
2 Johnston, and Adrian Price-Whelan for valuable discussions
3 that shaped this paper.

4 AA and RES acknowledge support from the Research Cor-
5 poration through the Scialog Fellows program on Time Do-
6 main Astronomy, from NSF grant AST-2007232, and from
7 NASA grant 19-ATP19-0068. RES is supported in part by a
8 Sloan Fellowship. ECC acknowledges support for this work
9 provided by NASA through the NASA Hubble Fellowship
10 Program grant HST-HF2-51502 awarded by the Space Tele-
11 scope Science Institute, which is operated by the Association
12 of Universities for Research in Astronomy, Inc., for NASA,
13 under contract NAS5-26555. AW and MB received support
14 from: NSF via CAREER award AST-2045928 and grant AST-
15 2107772; NASA ATP grant 80NSSC20K0513; HST grants
16 AR-15809, GO-15902, GO-16273 from STScI.

17 This research is part of the Frontera computing project at
18 the Texas Advanced Computing Center (TACC). Frontera is
19 made possible by National Science Foundation award OAC-
20 1818253. Simulations in this project were run using Early
21 Science Allocation 1923870, and analyzed using computing
22 resources supported by the Scientific Computing Core at the
23 Flatiron Institute. This work used additional computational
24 resources of the University of Texas at Austin and TACC,
25 the NASA Advanced Supercomputing (NAS) Division and
26 the NASA Center for Climate Simulation (NCCS), and the
27 Extreme Science and Engineering Discovery Environment
28 (XSEDE), which is supported by National Science Founda-
29 tion grant number OCI-1053575.

30 AA would like to express sincere gratitude to ChatGPT for
31 its invaluable language assistance (and for writing its own
32 acknowledgment), and to OpenAI for providing the platform
33 and technology.

REFERENCES

- Aganze, C., Pearson, S., Starkenburg, T., et al. 2023, arXiv preprint arXiv:2305.12045
- Arora, A., Sanderson, R. E., Panithanpaisal, N., et al. 2022, *The Astrophysical Journal*, 939, 2
- Astropy Collaboration, Robitaille, T. P., Tollerud, E. J., et al. 2013, *A&A*, 558, A33, doi: [10.1051/0004-6361/201322068](https://doi.org/10.1051/0004-6361/201322068)
- Astropy Collaboration, Price-Whelan, A. M., Sipőcz, B. M., et al. 2018, *AJ*, 156, 123, doi: [10.3847/1538-3881/aabc4f](https://doi.org/10.3847/1538-3881/aabc4f)
- Astropy Collaboration, Price-Whelan, A. M., Lim, P. L., et al. 2022, *apj*, 935, 167, doi: [10.3847/1538-4357/ac7c74](https://doi.org/10.3847/1538-4357/ac7c74)
- Barry, M., Wetzel, A., Chapman, S., et al. 2023, *Monthly Notices of the Royal Astronomical Society*, stad1395
- Behroozi, P. S., Wechsler, R. H., & Wu, H.-Y. 2012a, *The Astrophysical Journal*, 762, 109
- Behroozi, P. S., Wechsler, R. H., Wu, H.-Y., et al. 2012b, *The Astrophysical Journal*, 763, 18
- Belokurov, V., Evans, N., Irwin, M., et al. 2007, *The Astrophysical Journal*, 658, 337
- Besla, G., Kallivayalil, N., Hernquist, L., et al. 2007, *The Astrophysical Journal*, 668, 949
- Bonaca, A., Hogg, D. W., Price-Whelan, A. M., & Conroy, C. 2019, *The Astrophysical Journal*, 880, 38
- Bovy, J. 2016, *Physical review letters*, 116, 121301
- Bovy, J., Erkal, D., & Sanders, J. L. 2017, *Monthly Notices of the Royal Astronomical Society*, 466, 628
- Caldwell, N., Bonaca, A., Price-Whelan, A. M., Sesar, B., & Walker, M. G. 2020, *The Astronomical Journal*, 159, 287
- Carlberg, R. 2009, *The Astrophysical Journal*, 705, L223
- Cleveland, W. S., & Devlin, S. J. 1988, *Journal of the American statistical association*, 83, 596
- Cohen, J. G., Sesar, B., Bahnolzer, S., et al. 2017, *The Astrophysical Journal*, 849, 150
- Collaboration, D., Aghamousa, A., Aguilar, J., et al. 2016a, *The DESI Experiment Part I: Science, Targeting, and Survey Design*. <https://arxiv.org/abs/1611.00036>
- Collaboration, G., Prusti, T., De Bruijne, J., et al. 2016b, *Astron. Astrophys*, 595, A1
- Collaboration, P., Ade, P., Aghanim, N., et al. 2015, XIII. *Cosmological parameters*
- Conroy, C., Naidu, R. P., Garavito-Camargo, N., et al. 2021, *Nature*, 592, 534
- Conroy, C., Bonaca, A., Cargile, P., et al. 2019, *The Astrophysical Journal*, 883, 107
- Cunningham, E. C., Deason, A. J., Sanderson, R. E., et al. 2019, *The Astrophysical Journal*, 879, 120
- Cunningham, E. C., Garavito-Camargo, N., Deason, A. J., et al. 2020, *The Astrophysical Journal*, 898, 4
- Dalton, G., Trager, S. C., Abrams, D. C., et al. 2012, in *Ground-based and Airborne Instrumentation for Astronomy IV*, Vol. 8446, SPIE, 220–231
- de Boer, T., Erkal, D., & Gieles, M. 2020, *Monthly Notices of the Royal Astronomical Society*, 494, 5315
- De Jong, R. S., Agertz, O., Berbel, A. A., et al. 2019, arXiv preprint arXiv:1903.02464
- Deason, A., Belokurov, V., Evans, N., et al. 2012, *Monthly Notices of the Royal Astronomical Society*, 425, 2840
- Deason, A. J., Wetzel, A. R., Garrison-Kimmel, S., & Belokurov, V. 2015, *Monthly Notices of the Royal Astronomical Society*, 453, 3568
- Erkal, D., & Belokurov, V. 2015a, *Monthly Notices of the Royal Astronomical Society*, 454, 3542
- . 2015b, *Monthly Notices of the Royal Astronomical Society*, 450, 1136
- Erkal, D., Belokurov, V., Bovy, J., & Sanders, J. L. 2016, *Monthly Notices of the Royal Astronomical Society*, 463, 102
- Erkal, D., Belokurov, V., Laporte, C., et al. 2019, *Monthly Notices of the Royal Astronomical Society*, 487, 2685
- Gaia, C., Brown, A., Vallenari, A., et al. 2018, *Astronomy & Astrophysics*, 616
- Garavito-Camargo, N., Besla, G., Laporte, C. F., et al. 2019, *The Astrophysical Journal*, 884, 51
- . 2021, *The Astrophysical Journal*, 919, 109
- Garrison-Kimmel, S., Wetzel, A., Bullock, J. S., et al. 2017, *Monthly Notices of the Royal Astronomical Society*, 471, 1709
- Garrison-Kimmel, S., Hopkins, P. F., Wetzel, A., et al. 2018, *Monthly Notices of the Royal Astronomical Society*, 481, 4133
- Green, S. B., van den Bosch, F. C., & Jiang, F. 2021, *Monthly Notices of the Royal Astronomical Society*, 503, 4075
- Grillmair, C. J. 2006, *The Astrophysical Journal*, 645, L37
- . 2009, *The Astrophysical Journal*, 693, 1118
- . 2017, *The Astrophysical Journal*, 834, 98
- Grillmair, C. J., & Dionatos, O. 2006, *The Astrophysical Journal*, 643, L17
- Harris, C. R., Millman, K. J., van der Walt, S. J., et al. 2020, *Nature*, 585, 357, doi: [10.1038/s41586-020-2649-2](https://doi.org/10.1038/s41586-020-2649-2)
- Hopkins, P. F. 2015, *Monthly Notices of the Royal Astronomical Society*, 450, 53
- Hopkins, P. F., Wetzel, A., Kereš, D., et al. 2018, *Monthly Notices of the Royal Astronomical Society*, 480, 800
- Horta, D., Cunningham, E. C., Sanderson, R. E., et al. 2023, *The Astrophysical Journal*, 943, 158
- Huber, P. J. 1973, *The annals of statistics*, 799
- Hunter, J. D. 2007, *Computing in Science and Engineering*, 9, 90, doi: [10.1109/MCSE.2007.55](https://doi.org/10.1109/MCSE.2007.55)
- Ibata, R., Malhan, K., Martin, N., et al. 2021, *The Astrophysical Journal*, 914, 123

- Ivezić, Ž., Kahn, S. M., Tyson, J. A., et al. 2019, *The Astrophysical Journal*, 873, 111
- Johnston, K. V., Spergel, D. N., & Haydn, C. 2002, *The Astrophysical Journal*, 570, 656
- Kallivayalil, N., van der Marel, R. P., Alcock, C., et al. 2006, *The Astrophysical Journal*, 638, 772
- Kazantzidis, S., Bullock, J. S., Zentner, A. R., Kravtsov, A. V., & Moustakas, L. A. 2008, *The Astrophysical Journal*, 688, 254
- Kim, S. Y., Peter, A. H. G., & Hargis, J. R. 2018, *PhRvL*, 121, 211302, doi: [10.1103/PhysRevLett.121.211302](https://doi.org/10.1103/PhysRevLett.121.211302)
- Koposov, S., Belokurov, V., Li, T., et al. 2019, *Monthly Notices of the Royal Astronomical Society*, 485, 4726
- Koposov, S. E., Erkal, D., Li, T. S., et al. 2023, *Monthly Notices of the Royal Astronomical Society*, 521, 4936
- Law, D. R., Johnston, K. V., & Majewski, S. R. 2005, *The Astrophysical Journal*, 619, 807
- Leitherer, C., Schaerer, D., Goldader, J. D., et al. 1999, *The Astrophysical Journal Supplement Series*, 123, 3
- Li, H., Hammer, F., Babusiaux, C., et al. 2021a, *The Astrophysical Journal*, 916, 8
- Li, T. S., Koposov, S. E., Erkal, D., et al. 2021b, *The Astrophysical Journal*, 911, 149
- Libeskind, N. I., Knebe, A., Hoffman, Y., et al. 2011, *Monthly Notices of the Royal Astronomical Society*, 411, 1525
- Lilleengen, S., Petersen, M. S., Erkal, D., et al. 2023, *Monthly Notices of the Royal Astronomical Society*, 518, 774
- Lowing, B., Jenkins, A., Eke, V., & Frenk, C. 2011, *Monthly Notices of the Royal Astronomical Society*, 416, 2697
- MacQueen, J. 1967, in *5th Berkeley Symp. Math. Statist. Probability*, University of California Los Angeles LA USA, 281–297
- Malhan, K., & Ibata, R. A. 2018, *Monthly Notices of the Royal Astronomical Society*, 477, 4063
- Malhan, K., Ibata, R. A., Carlberg, R. G., Valluri, M., & Freese, K. 2019, *The Astrophysical Journal*, 881, 106
- Malhan, K., Valluri, M., & Freese, K. 2021, *Monthly Notices of the Royal Astronomical Society*, 501, 179
- Mateu, C. 2023, *Monthly Notices of the Royal Astronomical Society*, stad321
- McMillan, P. J. 2016, *Monthly Notices of the Royal Astronomical Society*, stw2759
- Myeong, G., Jerjen, H., Mackey, D., & Da Costa, G. S. 2017, *The Astrophysical Journal Letters*, 840, L25
- Panithanpaisal, N., Sanderson, R. E., Wetzel, A., et al. 2021, *The Astrophysical Journal*, 920, 10
- Pawlowski, M. S., & Kroupa, P. 2020, *Monthly Notices of the Royal Astronomical Society*, 491, 3042
- Pearson, S., Clark, S. E., Demirjian, A. J., et al. 2022, *The Astrophysical Journal*, 926, 166
- Peñarrubia, J., Gómez, F. A., Besla, G., Erkal, D., & Ma, Y.-Z. 2015, *Monthly Notices of the Royal Astronomical Society: Letters*, 456, L54
- Perez, F., & Granger, B. E. 2007, *Computing in Science & Engineering*, 9, 21, doi: [10.1109/MCSE.2007.53](https://doi.org/10.1109/MCSE.2007.53)
- Petersen, M. S., & Peñarrubia, J. 2020, *Monthly Notices of the Royal Astronomical Society: Letters*, 494, L11
- Petersen, M. S., Weinberg, M. D., & Katz, N. 2022, *Monthly Notices of the Royal Astronomical Society*, 510, 6201
- Pietrzyński, G., Graczyk, D., Gallette, A., et al. 2019, *Nature*, 567, 200
- Power, C., Navarro, J. F., Jenkins, A., et al. 2003, *Monthly Notices of the Royal Astronomical Society*, 338, 14
- Price-Whelan, A. M., & Bonaca, A. 2018, *The Astrophysical Journal Letters*, 863, L20
- Robles, V. H., Kelley, T., Bullock, J. S., & Kaplinghat, M. 2019, *Monthly Notices of the Royal Astronomical Society*, 490, 2117
- Sales, L. V., Navarro, J. F., Kallivayalil, N., & Frenk, C. S. 2017, *MNRAS*, 465, 1879, doi: [10.1093/mnras/stw2816](https://doi.org/10.1093/mnras/stw2816)
- Salomon, J.-B., Libeskind, N., & Hoffman, Y. 2023, *Monthly Notices of the Royal Astronomical Society*, 523, 2759
- Samuel, J., Wetzel, A., Chapman, S., et al. 2021, *MNRAS*, 504, 1379, doi: [10.1093/mnras/stab955](https://doi.org/10.1093/mnras/stab955)
- Samuel, J., Wetzel, A., Tollerud, E., et al. 2020, *MNRAS*, 491, 1471, doi: [10.1093/mnras/stz3054](https://doi.org/10.1093/mnras/stz3054)
- Sanders, J. L., Bovy, J., & Erkal, D. 2016, *Monthly Notices of the Royal Astronomical Society*, 457, 3817
- Sanders, J. L., Lilley, E. J., Vasiliev, E., Evans, N. W., & Erkal, D. 2020, *Monthly Notices of the Royal Astronomical Society*, 499, 4793
- Sanderson, R. E., Wetzel, A., Loebman, S., et al. 2020, *The Astrophysical Journal Supplement Series*, 246, 6
- Santistevan, I. B., Wetzel, A., Tollerud, E., et al. 2023, *arXiv preprint arXiv:2309.05708*
- Savino, A., Weisz, D. R., Skillman, E. D., et al. 2022, *The Astrophysical Journal*, 938, 101
- Shapiro, S. S., & Wilk, M. B. 1965, *Biometrika*, 52, 591
- Spergel, D., Gehrels, N., Breckinridge, J., et al. 2013, *arXiv preprint arXiv:1305.5422*
- Spergel, D., Gehrels, N., Baltay, C., et al. 2015, *arXiv preprint arXiv:1503.03757*
- Takada, M., Ellis, R. S., Chiba, M., et al. 2014, *Publications of the Astronomical Society of Japan*, 66, R1
- van den Bosch, F. C., Ogiya, G., Hahn, O., & Burkert, A. 2018, *Monthly Notices of the Royal Astronomical Society*, 474, 3043
- Vasiliev, E. 2019, *Monthly Notices of the Royal Astronomical Society*, 482, 1525
- Vasiliev, E. 2023, *Galaxies*, 11, 59, doi: [10.3390/galaxies11020059](https://doi.org/10.3390/galaxies11020059)
- Vasiliev, E. 2023, *arXiv preprint arXiv:2306.04837*

- Vasiliev, E., Belokurov, V., & Erkal, D. 2021, Monthly Notices of the Royal Astronomical Society, 501, 2279
- Virtanen, P., Gommers, R., Oliphant, T. E., et al. 2020, Nature Methods, 17, 261, doi: [10.1038/s41592-019-0686-2](https://doi.org/10.1038/s41592-019-0686-2)
- Vogelsberger, M., Zavala, J., & Loeb, A. 2012, Monthly Notices of the Royal Astronomical Society, 423, 3740
- Weinberg, M. D. 2022, arXiv e-prints, arXiv:2209.06846. <https://arxiv.org/abs/2209.06846>
- Wes McKinney. 2010, in Proceedings of the 9th Python in Science Conference, ed. Stéfan van der Walt & Jarrod Millman, 56 – 61, doi: [10.25080/Majora-92bf1922-00a](https://doi.org/10.25080/Majora-92bf1922-00a)
- Wetzel, A., & Garrison-Kimmel, S. 2020a, HaloAnalysis: Read and analyze halo catalogs and merger trees. <http://ascl.net/2002.014>
- . 2020b, GizmoAnalysis: Read and analyze Gizmo simulations. <http://ascl.net/2002.015>
- Wetzel, A., Hayward, C. C., Sanderson, R. E., et al. 2023, The Astrophysical Journal Supplement Series, 265, 44
- Wetzel, A. R., Deason, A. J., & Garrison-Kimmel, S. 2015, The Astrophysical Journal, 807, 49
- Wetzel, A. R., Hopkins, P. F., Kim, J.-h., et al. 2016, The Astrophysical Journal Letters, 827, L23
- Wilks, S. S. 1938, Psychometrika, 3, 23
- Williams, M. E., Steinmetz, M., Sharma, S., et al. 2011, The Astrophysical Journal, 728, 102
- Yam, W., Carlin, J. L., Newberg, H. J., et al. 2013, The Astrophysical Journal, 776, 133
- Yoon, J. H., Johnston, K. V., & Hogg, D. W. 2011, The Astrophysical Journal, 731, 58
- Zonca, A., Singer, L. P., Lenz, D., et al. 2019, Journal of Open Source Software, 4, 1298

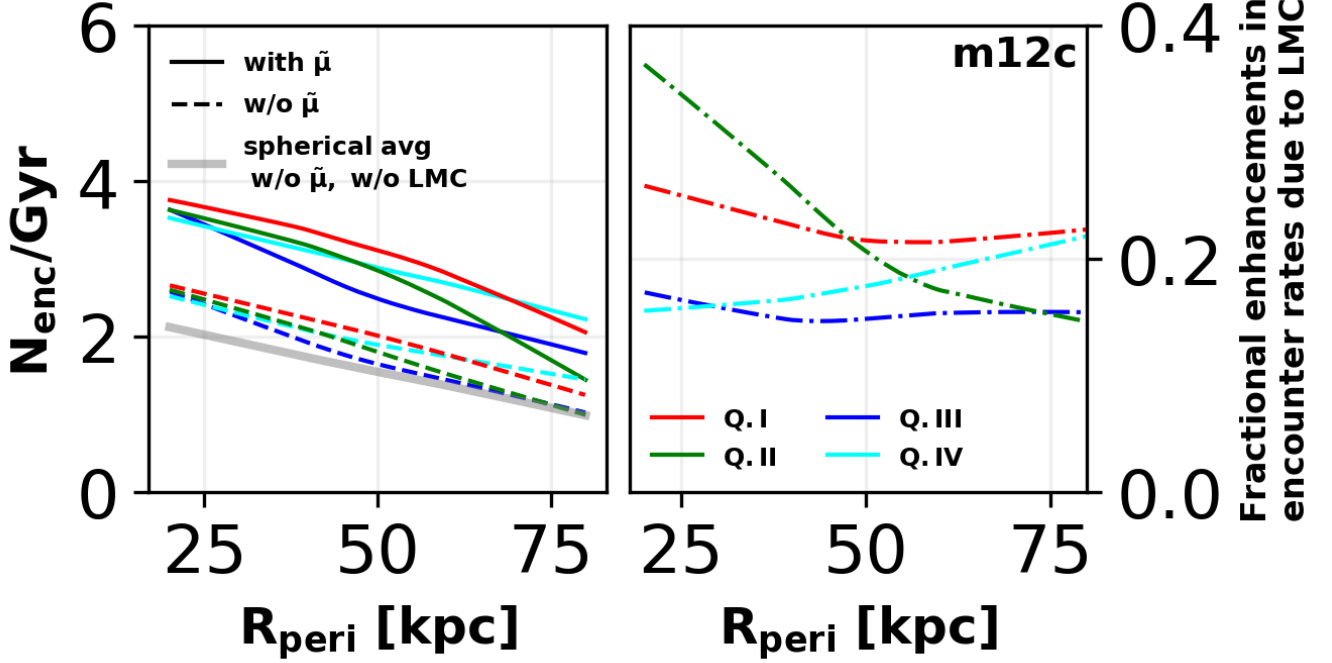


Figure 14. Encounter rates in Sec.4.1 for m12c, assuming $T = 0$ Gyr when the LMC-analog is at a distance of 50 kpc from the host center. Left: Estimated number of encounters per Gyr for a synthetic stream of length $\ell_s = 10$ kpc and impact parameter $b_{\max} = 1$ in m12c with $\tilde{\mu}$ (solid) and w/o $\tilde{\mu}$ (dashed) plotted as a function of the stream’s pericenter distance at $T=0$ Gyr and four quadrants (marked by colors) (compared to Fig. 10). The gray line represents the range of encounter rates for m12c w/o $\tilde{\mu}$ and w/o contributed subhalos, averaged over all quadrants. Highest encounter rates occur Q.I and Q.IV (where the LMC-analog orbits in integration time frame). Right: Fractional enhancements of encounter rates due to contributed subhalos from the LMC-analog for m12c (compared to Fig. 11). Q.I and Q.IV exhibit a consistent 20% increase in encounter rates in the outer halo due to higher subhalo density around and trailing behind the analog. In contrast, Q.II shows the highest enhancements in the inner regions (up to 35%) due to leading contributed subhalos along the future orbit of the LMC-analog in m12c.

APPENDIX

1. Encounter rates in another LMC-analog (m12c)

In this appendix, we repeat our analysis from Sec. 4.1. We achieve this by injecting and integrating 5000 synthetic stream orbits, as described in Sec. 2.5 in the context of m12c, which has *another* LMC-analog, with first pericentric passage about 1 Gyr before the present day, at a much closer distance of about 18 kpc. Following Barry et al. (2023), we assume $T = 0$ Gyr (first pericentric passage), when the LMC-analog is 50 kpc away from the center. The LMC-analog’s orbit largely lies in the disc plane until the $T = 0.2$ Gyr. During this time, the analog starts in Q.IV and move inwards with the first pericenter ($T = 0$ Gyr) into Q.I. The actual pericenter occurs in Q.II at $T = 0.15$ Gyr. We integrate our synthetic stream orbits from -0.4 Gyr to 0 Gyr (in contrast to -0.4 Gyr to 0.1 Gyr in the m12b case) and do not anticipate significant north–south asymmetry (collective response) or the emergence of reflex motion during this period, given that the LMC remains within the plane of the galactic disc.

The left panel in Fig. 14 shows the average encounter rates of synthetic streams as function of their pericentric distances in different quadrants (color-coded) within the context of m12c. A comparison with the encounter rates in m12b(Fig. 10) reveal an overall reduction by a factor of 1.6. This decrease is due to a higher number of subhalos in the MW 5 Gyr ago compared to 1 Gyr ago (see Fig. 4 in Barry et al. 2023). Notably, Q.I and Q.IV exhibit the highest encounter rates, aligning with the LMC-analog’s orbit and the expected DM wake. Q.II also displays some increased rates in the inner regions.

The right panel in Fig. 14 plots the fractional enhancements in $N_{\text{enc}}/\text{Gyr}$ due to contributed subhalos in m12c. Even though both the LMC-analogs (in m12c and m12b) start with the same number of subhalos, the overall enhancements in m12c are higher than m12b (Fig. 11) due to decreased total subhalo population at later times. Q.I and Q.II exhibit a consistent enhancements of 30% or more in the inner regions due to leading subhalos following the analog’s future orbit, while Q.I and Q.IV both experience over 20% increase in the outer halo. While the total fractional enhancement for real LMC is more accurate for m12c, given its

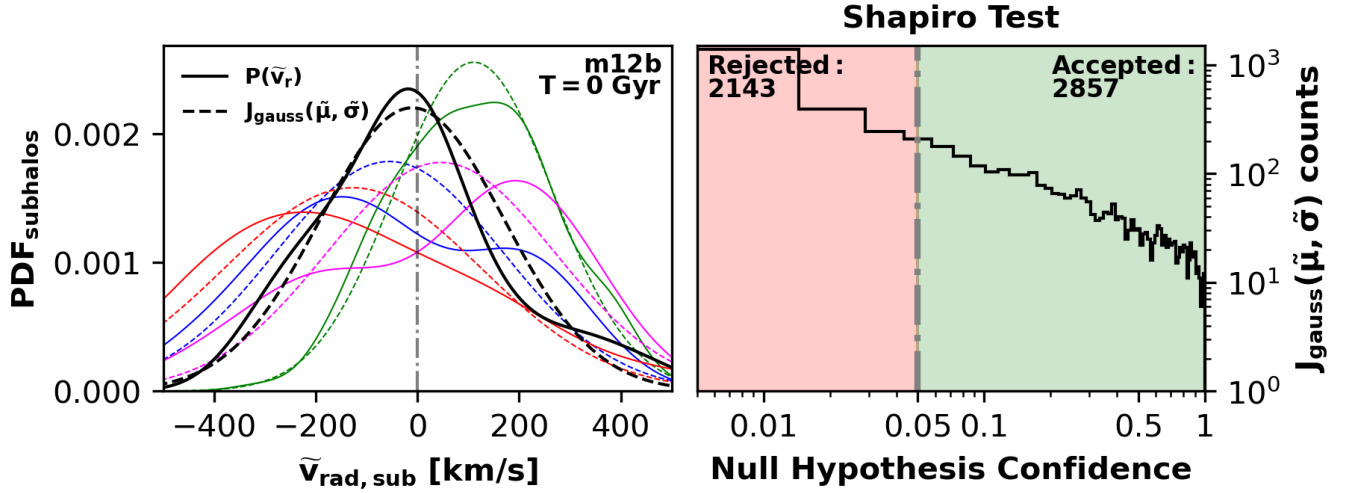


Figure 15. Left: Probability density function (PDF) of radial velocity $P(\tilde{v}_r)$ in stream-centric coordinates (solid lines), along with corresponding Gaussian distribution fits $J_{\text{gauss}}(\tilde{\mu}, \tilde{\sigma})$ (dashed lines) for a representative sample of MW streams in m12b, illustrated with different colors at $T = 0$ Gyr. This comparison visually attests to the adequacy of Gaussian approximation. Right: Histogram of computed p-values obtained through the Shapiro-Wilk test (Shapiro & Wilk 1965), which assesses the null hypothesis of normal distribution. Applied to the PDF of subhalos’ radial velocity $P(\tilde{v}_r)$ in stream-centric coordinates for all 5000 synthetic streams in m12b at $T = 0$ Gyr. The red-shaded region indicates the 0.05 significance threshold, below which the null hypothesis is rejected. Conversely, green-shaded regions denote acceptance. Over 50 % of PDFs analyzed follow Gaussianity from the accepted number of samples.

LMC-analog’s proximity to the present day, it’s important to note that the quadrant and distance dependencies are highly sensitive to the orbit and pericentric distance, making m12b more suitable for predicting regions of enhancements from the real LMC .

2. Gaussianity Analysis of Subhalos’ Radial Velocity Distributions

In this appendix, we investigate the Gaussianity assumption underlying the Probability Density Function (PDF) for subhalos’ radial velocity $P(\tilde{v}_r)$ in stream-centric coordinates. This assumption plays a crucial role in deriving an analytical model for subhalo-stream encounter rates, as expressed in Eq. 13.

The encounter rate are directly dependent on the stream-subhalo kinematics, primarily characterized by the Gaussian parameters—the mean radial velocity ($\tilde{\mu}$) and dispersion ($\tilde{\sigma}$) in stream-centric coordinates. Consequently, we examine the validity of assuming a Gaussian distribution $J_{\text{gauss}}(\tilde{\mu}, \tilde{\sigma})$ for $P(\tilde{v}_r)$. It is noteworthy that the PDFs subjected to analysis in this section exclusively concern subhalos positioned around streams, in accordance with the description provided in Sec. 2.4. Our analysis concentrates on these PDFs and their corresponding Gaussian fits within the context of the m12b at $T = 0$ Gyr. This specific choice is motivated by the fact that the LMC-analog’s first pericentric passage induces significant perturbations on the Gaussianity assumption, owing to its pronounced dipolar moment (Petersen & Peñarrubia 2020; Cunningham et al. 2020).

The left panel of Fig. 15 shows $P(\tilde{v}_r)$ (solid lines) and their corresponding Gaussian fits (dashed lines) for a representative set of MW streams (varied colors). Notably, the means of different PDFs and their fits display similar trends. It’s important to note that this mean value can shift, either towards more negative or positive values, thereby leading to the conditions $f(\gamma) \geq 1$ or $f(\gamma) \leq 1$ (see Fig.4) respectively. This shift’s potential influence on the scaling factor behavior is highlighted. The alignment between Gaussian distributions and actual PDFs visually confirms the Gaussian fitting assumption.

For a quantitative evaluation, we subject the Gaussian assumption to a rigorous test using the Shapiro-Wilk test (Shapiro & Wilk 1965) on the PDFs of 5000 synthetic streams. This statistical test evaluates the null hypothesis of Gaussian distribution for each $P(\tilde{v}_r)$.

The right panel of Fig. 15 depicts a histogram of computed p-values (Null hypothesis confidence) from the Shapiro-Wilk test. The red-shaded region identifies the 0.05 significance threshold, marking p-values below which the null hypothesis is rejected. Among the analyzed distributions, 2143 exhibit p-values below 0.05 (non-Gaussian behavior), while 2857 distributions show p-values above 0.05 (green region), reinforcing the Gaussian assumption as over 50% of the distributions have p-values in the green region.

Remarkably, the p-value counts demonstrate logarithmic decrease, highlighting a gradual transition from non-Gaussian to Gaussian behavior in the PDFs. This observation further endorses the Gaussian approximation’s appropriateness for the PDFs.